1

Determining the effect of varying magmatic volatile content on lunar magma ascent dynamics

Lo M.[1], La Spina G.[1], Joy K.H.[1], Polacci M.[1], and Burton M.[1]

[1]Department of Earth and Environmental Sciences, University of Manchester, Williamson Building, Oxford Road, Manchester, M13 9PL, UK

Corresponding author: Marissa Lo (marissa.lo@manchester.ac.uk)

Key Points:

- We use a magma ascent model and sensitivity analysis to understand the relative significance of different volatiles on lunar magma ascent.

- For the range of initial volatile abundances considered, CO and H_2 were more significant than H_2O in driving lunar magma ascent.

- Results highlight the importance of quantifying and determining the origin of CO, and understanding H-speciation within the lunar mantle.

Abstract

The Moon is not volcanically active at present, therefore, we rely on data from lunar samples, remote sensing, and numerical modelling to understand past lunar volcanism. The role of different volatile species in propelling lunar magma ascent and eruption remains unclear. We adapt a terrestrial magma ascent model for lunar magma ascent, considering different compositions of picritic magmas and various abundances of H_2, H_2O, and CO (measured and estimated) for these magmas. We also conduct a sensitivity analysis to investigate the relationship between selected input parameters (pre-eruptive pressure, temperature, conduit radius, volatile content) and given outputs (exit gas volume fraction, velocity, pressure, and mass eruption rate,). We find that, for the model simulations containing H_2O and CO, CO was more significant than H_2O in driving lunar magma ascent, for the range of volatile contents considered here. For the simulations containing H_2 and CO, H_2 had a similar or slightly greater control than CO on magma ascent dynamics. Our results showed that initial H_2 and CO content has a strong control on exit velocity and pressure, two factors that strongly influence the formation of an eruption plume, pyroclast ejection, and overall deposit morphology. Our results highlight the importance of (1) quantifying and determining the origin of CO, and (2) understanding the abundance of different H-species present within the lunar mantle. Quantifying the role of volatiles in driving lunar volcanism provides an important link between the interior volatile content of the Moon and the formation of volcanic deposits on the lunar surface.

Plain Language Summary

Unlike the Earth, the Moon does not have any active volcanoes, and hasn't had any active volcanoes for at least the last 100 million to 1 billion years. Therefore, we rely on studying samples collected by astronauts and robotic landers, satellite data, and computer models to understand what volcanic activity on the Moon was like. Volcanic eruptions are mostly driven by gas: as magma rises in the Moon's crust, gases will separate out, allowing magma to rise more quickly. As a result of this, we can use volcanic eruptions to understand how much gas exists within the Moon, which is important for understanding how the Moon formed. We used a computer model to simulate magma ascent on the Moon in order to understand what gases were more significant in driving magma ascent. We found that molecular hydrogen and carbon monoxide had a bigger effect on magma ascent than water, so would have a greater effect on the style of volcanic eruptions on the Moon. The source of carbon monoxide and the relative amounts of molecular hydrogen and water in the Moon's mantleare currently unknown and our results highlight the importance of understanding this information for understanding lunar volcanic activity.

1 Introduction

1.1 Lunar pyroclastic deposits

Volcanism is a key process that links the interior of a planetary body to its surface, and therefore understanding lunar volcanic processes can help us understand the volatile content of the lunar interior [Anand et al., 2014; Grove and Krawczynski, 2009; Rutherford et al., 2017]. Data from lunar samples, remote sensing, and modelling are key tools in understanding lunar volcanism [Basaltic Volcanism Study Project, 1981; Jolliff et al., 2006].

Lunar pyroclastic glass beads have been a significant source of information for studying volcanic activity on the Moon [Elkins-Tanton, 2003a]. Pyroclastic material has been found on

59 the surface of the Moon in many of the returned lunar soil samples [Delano et al., 1986; Heiken
60 et al., 1974] and via remote sensing data [Carter et al., 2009; Gaddis et al., 1985; Hawke et al.
61 1989]. Not only do these pyroclastic glass beads provide evidence that the Moon experienced
62 explosive volcanism, rather than solely effusive volcanism [Coombs and Hawke, 1992; Morgan
63 et al., 2021; Wilson and Head, 1981], they have also been important samples for researching the
64 volatile content of the Moon's mantle [Saal et al., 2008; Hauri et al., 2011]. These pyroclasts are
65 picritic in composition (containing <52 wt % SiO_2 and >12 wt % MgO [Le Bas, 1999]),
66 spherical to ovoid in shape, occasionally host olivine phenocrysts [Hauri et al., 2011], have a
67 glassy or devitrified texture, and are analogous to terrestrial Pele's tears [Moune et al., 2007].
68 Based on the lack of impact metamorphic shock textures and textural and chemical homogeneity,
69 it has been largely accepted that these pyroclastic glass beads were produced by explosive
70 volcanic activity [Carter et al., 2009; Coombs and Hawke, 1992; Weitz et al., 1998].
71 Compositionally, the pyroclastic glasses are grouped by their TiO_2 content, from very low-Ti (<
72 1% TiO_2), to low-/intermediate-Ti (1-6% TiO_2), to high-Ti (> 6% TiO_2), which correspond to the
73 colours green, yellow, and orange/red/black respectively [Neal and Taylor, 1992].

74   The pyroclastic glass beads have been observed as a component within the regolith at all
75 Apollo landing sites [Delano, 1986; Heiken et al., 1974], but are also found in concentrated
76 deposits. These concentrated deposits of pyroclastic glass beads are termed dark mantling
77 deposits, based on their low albedo in spectral data and interaction with pre-existing topography
78 [Gaddis et al., 1985; Gaddis et al., 2003]. Over 100 dark mantling deposits have now been
79 identified across the Moon, with the majority of these located on the lunar nearside [Gustafson et
80 al., 2012]. These deposits have been categorised by their areal extent as local (~250-550 km^2) or
81 regional (> 1000 km^2), with a roughly equal number of deposits split between these two
82 categories [Gaddis et al., 2000; Weitz et al., 1998]. It has been widely agreed that the volcanic
83 eruptions that produced the picritic glass beads were analogous to lava fountain eruptions [Carter
84 et al., 2009; Coombs and Hawke, 1992; Elkins-Tanton et al., 2003a], with localised and regional
85 dark mantling deposits produced by eruptions equivalent to terrestrial Vulcanian and
86 Strombolian eruption styles respectively [Head and Wilson, 1979].

87   1.2 Measuring volatiles in lunar pyroclastic glass beads

88   The discovery of measurable amounts of H in lunar pyroclastic glasses and melt
89 inclusions [Hauri et al., 2011; Saal et al., 2008] led to a paradigm shift from viewing the Moon's
90 mantle as dry [Shearer et al., 2006] to relatively wet, likely heterogeneously so [McCubbin et al.,
91 2015]. Many studies have followed this discovery, aiming to quantify the abundance of H (as OH
92 and equivalent H_2O) and other volatiles in the lunar mantle [Boyce et al., 2010; Hauri et al.,
93 2011; Tartèse et al., 2014; Wang et al., 2012]. The huge body of research dedicated to
94 understanding H_2O and other volatiles in the lunar interior has clear implications for
95 understanding the formation, thermal history, and volcanic history of the Moon [Anand et al.,
96 2014; Hartmann, 2014; Hartmann and Davis, 1974].

97   While progress has been made in quantifying lunar volatiles from lunar samples, it is still
98 not clear what role different volatile elements had during magma ascent and volcanic eruptions
99 on the Moon. Since the Moon has not been volcanically active for at least 100 Ma [Braden et al.,
100 2014], likely not for the last 1 Ga [Hiesinger et al., 2011], it is difficult to understand past active
101 volcanic processes. To this aim, numerical models of magma ascent provide an invaluable tool to
102 investigate and understand the processes and dynamics that occurred during volcanic eruptions.

103   1.3 Magma ascent modelling

104   Magma ascent is a complex process since it comprises numerous, interrelated processes
105 that have significant effects, such as crystallisation, degassing, temperature, pressure, and
106 rheological changes [La Spina et al., 2015]. Individually, each of these processes can already
107 have a significant effect on magma ascent dynamics [Caricchi et al., 2007; Dingwell and Webb,
108 1989; Sigurdsson, 2015; Webb and Dingwell, 1990]. However, they can also affect each other in
109 non-linear ways, producing feedbacks and interactions we cannot readily anticipate by studying
110 them separately. An example of this is the temperature within the conduit, which is affected by
111 both the adiabatic cooling due to bubble expansion and by the heating resulting from the release
112 of latent heat of crystallisation [La Spina et al., 2015]. The temperature resulting from the
113 balance of these processes then affects the rheology of magma, which, in turn, alters the velocity
114 of ascent. This influences the time available for crystals to grow, and, consequently, the release
115 of latent heat, producing a feedback on the temperature itself, which can be only quantified by
116 considering all these processes simultaneously. Overall, it is extremely important to incorporate
117 all of these processes into a holistic, quantitative, and comprehensive model for magma ascent.

118   Early models for magma ascent on Earth and on the Moon did not account for the
119 presence of multiple gas phases, crystals, gas-magma separation, or temperature variation
120 [Wilson, 1980; Wilson and Head, 1981]. Over time, models began to consider the presence of
121 crystals [Papale and Dobran, 1994], the presence of multiple gas phases [Papale, 1999; Papale,
122 2001], and variations in source temperature [Costa et al., 2007; Melnik and Sparks, 2002],
123 although these additional complexities have mostly been confined to terrestrial magma ascent
124 models rather than lunar magma ascent models. Most models for lunar magma ascent have either
125 been theoretical [Wilson and Head, 2017] or focussed more on the rock mechanics aspect of
126 magma ascent [Lister and Kerr, 1991; Wilson and Head, 2003] rather than the magmatic aspect.
127 Numerical models for lunar magma ascent have been explored, such as in Rutherford and Papale
128 (2009), where they modelled the ascent of an intermediate- to high-Ti, orange picrite from 8 km
129 depth to the lunar surface, using a fixed temperature. Through this, they were able to quantify the
130 gas volume fraction during ascent and the exit velocity, as well as predict that magma
131 fragmentation would occur once the magma reached the lunar surface.

132   To investigate the role of different volatile species (H_2, H_2O, and CO) on lunar magma
133 ascent, we use a numerical model for terrestrial magma ascent [Aravena et al., 2018; Carr et al.
134 2018; de' Michieli Vitturi et al., 2011; La Spina et al., 2015, 2021], that has been adapted for the
135 Moon. The model we present here incorporates the parameters and processes mentioned above,
136 providing a holistic approach, where the petrological, thermodynamic, rheological, and
137 degassing processes are all addressed, quantified, and combined together.

138   Overall, in this study we aim to (1) quantify the effect of varying magmatic volatile
139 content on magma ascent dynamics on the Moon, (2) understand the relative importance of
140 different magmatic volatiles on magma ascent dynamics, and (3) compare and contrast our
141 results with existing models for lunar magma ascent.

142 **2 Methods**

143   2.1 Model background

144   Here we used a 1-dimensional, multiphase, steady-state Fortran 90-based model for the
145 ascent of magma in a cylindrical conduit [Aravena et al., 2018; Carr et al. 2018; de' Michieli

146 Vitturi et al., 2011; La Spina et al., 2015, 2021]. The magma ascent model consisted of a system
147 of partial differential equations derived from the work of Romenski et al. (2010), which coupled
148 conservation equations for mass, momentum, and energy of the whole mixture, with balance
149 equations describing the evolution of the internal phases within the mixture (such as the
150 evolution of volume and mass fractions and of the gas/liquid slip velocity). The governing
151 equations of the 1D steady-state magma ascent model adopted here are reported in Text S1 of the
152 Supporting Information.

153 Providing constitutive equations (such as appropriate rheological, crystallisation, and
154 exsolution models), equations of state of each phase, boundary conditions (such as fixed pressure
155 or choked flow condition at the vent of the conduit), and input parameters (such as inlet pressure
156 and temperature, radius of the conduit, volatile content, and crystal content), the magma ascent
157 model calculated several quantities within the entire conduit and at the exit vent (such as
158 pressure, temperature, ascent velocity, gas content, crystal content, and viscosity).

159 The model is versatile and numerous versions have previously been used to address
160 several volcanological questions, such as the complex variation of temperature within a conduit
161 as a result of decompression and gas expansion (which induce a cooling of the magmatic
162 mixture) and crystallisation (which causes a heating of the magmatic mixture) during the ascent
163 of a basaltic magma [La Spina et al., 2015]. The model has also been used to constrain
164 characteristic times of crystallisation and exsolution [La Spina et al., 2016], showing that syn-
165 eruptive crystallisation during effusive and mild lava fountaining requires about two hours to
166 reach equilibrium. Recently, Arzilli et al. (2019) used this magma ascent model to show that a
167 rapid magma ascent during basaltic explosive eruptions (such as Plinian or sub-Plinian eruptions)
168 produces a large undercooling. By performing fast-cooling synchrotron experiments, they found
169 that this large undercooling can induce rapid syn-eruptive crystallisation on the order of minutes,
170 and not hours, as for mild lava fountaining activity, increasing viscosity and leading eventually
171 to explosive magma fragmentation. A different version of the model, which considers lateral
172 degassing, has been used by Carr et al. (2018) to calculate the extrusion and ascent rate of
173 magma during the 2006 effusive eruption of Merapi, Indonesia. Furthermore, following de'
174 Michieli Vitturi et al. (2010), Aravena et al. (2017, 2018) modified the model to allow conduit
175 radius variations with depth in order to investigate conduit stability during explosive eruptions.

176 2.2 Test case scenarios

177 We investigated the role of volatiles on magma ascent dynamics on the Moon by
178 considering the main five compositions of lunar picritic magmas (Table 1): green (very low-
179 TiO_2), yellow (low- to intermediate-TiO_2), and orange, red, and black (high-TiO_2).

180 Geochemical data has indicated that lunar picritic glass beads originate from a magma
181 that underwent very little fractional crystallisation, since they are enriched in Mg and Ni,
182 compatible elements that are usually incorporated into common minerals, like olivine [Taylor et
183 al., 1991]. As a result, picritic pyroclastic glass beads represent primary partial melting of lunar
184 mantle, representing the most primitive lunar material [Hess, 2000; Shearer and Papike, 1993].
185 Hughes et al. (1988) modelled the best fit source region compositions for Apollo 15 green
186 pyroclastic glasses and produced an estimate of between 4 to 7% partial melting of mafic
187 cumulates. Shearer and Papike (1993) also found that mare basalts and picritic pyroclastic
188 glasses do not lie on the same liquid line of descent or crystallisation path of cooling – indicating
189 that they originated from source regions of different depths. The source depth of the picritic

190 glasses has previously been calculated using phase relationships and experimental petrology
191 [Delano, 1980]. Brown and Grove (2015) used high-pressure, high-temperature pistons to
192 determine the conditions under which intermediate-TiO_2, yellow picritic glass beads would be in
193 equilibrium with different cumulate minerals. It was concluded that olivine and low-Ca pyroxene
194 cumulates would be in equilibrium with the picritic melts at pressures of 2.4 to 3.0 GPa,
195 equivalent to lunar mantle depths of 512 to 646 km. Furthermore, by analysing the volatile
196 phases present in Apollo 15 green glass beads, Elkins-Tanton et al. (2003b) proposed that the
197 glasses originated from pressures of roughly 2.2 GPa, corresponding to roughly 450 km depth.

198 ### 2.3 Constitutive equations

199 The constitutive equations of the magma ascent model relate the governing equations to a
200 specific magmatic system, in this case, the ascent of picritic magmas within the lunar crust (see
201 Text S1 of Supporting Information). With respect to constitutive equations previously used by La
202 Spina et al. (2015, 2016, 2017, 2019, 2021) to simulate magma ascent at Stromboli, Etna,
203 Kilauea, and Sunset Crater volcanoes, we modified the rheological model to consider the
204 composition of the lunar picritic magmas described in section 2.2. We also considered different
205 volatile components (see below) and the corresponding solubility models. The new constitutive
206 equations adopted in this work are described in the sections below (see Table S1 of Supporting
207 Information for symbols used in equations).

208 The friction with the wall of the conduit was modelled as a function of the Reynolds
209 number, as detailed in La Spina et al. (2019). Laminar and turbulent flows were considered with
210 the corresponding friction factors according to the flow regime [Colebrook, 1939; Fang et al.,
211 2011, La Spina et al., 2019]. We assumed a constant crystal content of 1 vol.% in agreement with
212 calculations completed using MELTS [Ghiorso and Gualda, 2015; Gualda et al., 2012]: see Text
213 S2 and Datasets S1-2 of Supporting Information. For fragmentation, we utilised the strain rate
214 model by Papale (1999), which suggests that fragmentation would occur when the Deborah
215 number, the ratio between the Maxwell relaxation time and the timescale of deformation [Webb
216 and Dingwell, 1990], exceeds the critical value of 0.01. For outgassing, we adopted a permeable
217 gas flow regime using the Forchheimer's law to describe outgassing below the fragmentation
218 depth [Degruyter et al., 2012; La Spina et al., 2017], while the drag model for gas-ash flow
219 illustrated by Yoshida and Koyaguchi (1999) was used above the fragmentation depth. Finally,
220 the gravitational acceleration was changed from 9.81 m s^{-2} to 1.62 m s^{-2}, reflecting the
221 gravitational force on the Moon.

222 ### 2.3.1 Rheology

223 The viscosity was calculated using the Costa (2005) model:

$$\mu_l = \mu_{melt} \cdot \theta_c \cdot \theta_b, \tag{1}$$

224 where μ_l is the viscosity of the magma, μ_{melt} is the viscosity of the bubble-free, crystal-
225 free liquid phase, θ_c is a factor that increases viscosity due to the presence of crystals, and θ_b is a
226 factor that takes into account the effect of bubbles on the magmatic mixture. To estimate μ_{melt}
227 we adopted the viscosity model of Giordano et al. (2008), using the melt compositions for lunar
228 magmas reported in Table 1.

229 The presence of crystals was accounted for by θ_c as described in Costa (2009):

$$\theta_c = \frac{1 + \varphi^\delta}{[1 - F(\varphi, \xi, \gamma)]^{B\phi^*}}, \tag{2}$$

230   where

$$F = (1 - \xi)erf\left[\frac{\sqrt{\pi}}{2(1 - \xi)}\varphi(1 + \varphi^\gamma)\right], \quad \varphi = \frac{\left(\sum_{j=1}^{n_c} x_{c_j}^l\right)}{\phi^*}. \tag{3}$$

231   The fitting parameters B, δ, ξ, γ and ϕ^* chosen for this work are the same used in
232   Giordano and Dingwell (2003): $B = 2.8, \delta = 13 - \gamma, \xi = 0.0327, \gamma = 0.84$.

233   The relative viscosity due to the presence of bubbles was calculated using the general formula by
234   Llewellin et al. (2002) and Mader et al. (2013):

$$\theta_b = \theta_{b,\infty} + \frac{\theta_{b,0} - \theta_{b,\infty}}{1 + (K\,Ca)^m} \tag{4}$$

$$\theta_{b,0} = \left(1 - \alpha_g\right)^{-1} \tag{5}$$

$$\theta_{b,\infty} = \left(1 - \alpha_g\right)^{\frac{5}{3}} \tag{6}$$

235   where K = 6/5 and m = 2.

236

237   Table 1: Melt compositions used in model, based on geochemical data from the Apollo 11, 15,
238   and 17 picritic glass beads [Binder, 1976; Delano and Lindsley, 1983; Delano and Livi, 1981;
239   Shearer et al., 1990; Shearer and Papike, 1993]. A dashed line means that the data was not
240   reported.

Oxide/ wt. %	Green (Very low-Ti)	Yellow (Low- to Intermediate-Ti)	Orange (High-Ti)	Red (High-Ti)	Black (High-Ti)
SiO_2	45.6	40.5	39.2	33.8	33.9
TiO_2	0.43	7.0	9.0	16.3	16.1
Al_2O_3	7.5	8.2	7.3	4.8	4.4
FeO	19.2	22.2	22.4	23.9	22.5
MnO	0.26	0.24	0.28	0.33	0.25
MgO	17.9	12.2	12.4	13.2	13.8
CaO	8.3	8.8	8.3	6.8	6.4
Na_2O	0.16	0.4	0.4	0.1	0.8
K_2O	0.01	-	0.05	0.175	0.400
P_2O_5	0.03	-	-	-	-
Total	98.96	99.54	99.33	99.405	98.55
Sources	Average of 17 Apollo 15 samples [Binder, 1976; Shearer and	Average of 11 samples from Apollo 17 [Delano and Lindsley, 1983].	Average of 61 samples from Apollo 17 [Delano	Average of 4 samples from Apollo 12 [Delano and Livi, 1981; Shearer and	Average of 7 samples from Apollo 14 [Shearer et al., 1990].

	Papike, 1993].		and Lindsley, 1983].	Papike, 1993].	

241   2.3.2 Volatile solubility

242   The magma ascent model is able to account for two volatile species; we consider the
243   combinations of H_2O and CO and H_2 and CO throughout this study. Renggli et al. (2017)
244   calculated the relative abundance of various H, O, C, Cl, S, and F-based species in picritic
245   magmas to determine the overall composition of the volcanic gas emitted during an explosive
246   lunar eruption. The study highlighted that the redox conditions present within the lunar mantle
247   are a key control on the type of H-speciation, controlled by the depletion of different volatiles
248   and metals during the formation of the Moon. We know that the lunar mantle has very reducing
249   conditions, with estimates of the oxygen fugacity ranging from +0.2 to −2.5 log units from the
250   iron-wüstite buffer [Fogel and Rutherford, 1995; Shearer and Papike, 2004; Nicholis and
251   Rutherford, 2009]. Renggli et al. (2017) concluded that the most abundant gases would be, in
252   descending order of abundance, CO, H_2, H_2S, COS, and S_2, while H_2O was one of the more
253   minor H-species, a result that is consistent with other authors [Sharp et al., 2011].

254   Using measurements of carbon in lunar volcanic glasses and melt inclusions from Apollo
255   15 and 17 samples, Wetzel et al. (2015) demonstrated that carbon is present as a dissolved
256   species in lunar magmas. A large number of authors have previously identified CO as a key
257   volatile for driving lunar volcanism and have attributed the production of CO in the lunar mantle
258   to the oxidation of graphite [Fogel and Rutherford, 1995; Nicholis and Rutherford, 2009;
259   Rutherford and Papale, 2009; Sato, 1979; Spudis, 2015; Wetzel et al., 2015; Wilson and Head,
260   2017]. However, graphite has not been detected within any lunar samples as an igneous phase
261   [McCubbin et al., 2015]; the only recorded occurrence of graphite has been within an Apollo 17
262   breccia associated with impact melting [Steele et al., 2010]. Fogel and Rutherford (1995)
263   proposed that CO was produced by reactions between C and Fe-, Cr-, and Ti-oxides in the melt;
264   reactions such as this could produce up to 1000 ppm of CO in low-Ti and intermediate-Ti
265   picrites. The direct dissolution of CO into magma as iron carbonyl ($Fe(CO)_5$) [Wetzel et al.,
266   2013] has also been proposed. Overall, the origin of CO within the lunar mantle remains
267   inconclusive. Organic sources of carbon have also been investigated, following the discovery of
268   complex organic matter on the surface of high-Ti, black pyroclastic glass beads [Thomas-Keprta
269   et al., 2014]. It was concluded that the source of the organic carbon is exogenous meteoritic
270   kerogen, delivered to the lunar regolith through micrometeorite impacts, therefore, it is unlikely
271   that this organic carbon would have played a role in magma ascent dynamics.

272   Although traces of H_2 have not been detected in the volatile-rich coatings of pyroclastic
273   glass beads, we consider H_2 in our magma ascent model as it is more likely to have been present
274   at depth in the mantle based on redox conditions within the lunar mantle [Sharp et al., 2011;
275   Renggli et al., 2017]. We also consider H_2O due to the greater amount of information available
276   on the behaviour of H_2O at high pressure and temperature, i.e. within the Earth's mantle. Several
277   papers present solubility models for H_2O under different conditions [Moore et al., 1995; Moore
278   et al., 1998; Mysen and Wheeler, 2000], whereas H_2 solubility models are less prevalent
279   [Hirschmann et al., 2012]. Using H_2O in our lunar magma ascent model is also useful from a
280   comparative planetology perspective, since H_2O is the dominant H-species within terrestrial
281   systems [Holloway and Blank, 1994].

282

283   Following La Spina et al. (2015), the mass fraction x_i^{melt} of the dissolved volatile
284 component i (i.e. H_2, H_2O, or CO) was calculated in the conduit model using the non-linear
285 solubility model:

286
$$x_i^{melt} = \sigma_i \left(\frac{P_i}{\bar{P}} \right)^{\epsilon_i}, \tag{7}$$

287 where P_i is the partial pressure, σ_i is a solubility coefficient, ϵ_i is a solubility exponent and $\bar{P} = 1$
288 Pa, a constant value used to make quantity in brackets adimensional.

289   To estimate both solubility exponents and coefficients for H_2O, we adopted the model of
290 Moore et al. (1998):

291
$$2 \ln X_{H_2O}^{melt} = \frac{a}{T} + \sum_i b_i x_i \left(\frac{P}{T} \right) + c \ln f_{H_2O}^{fluid} + d \tag{8}$$

292 where $X_{H_2O}^{melt}$ is the mole fraction of H_2O dissolved in the melt, $f_{H_2O}^{fluid}$ is the fugacity of H_2O in
293 the fluid, T is the temperature (Kelvin), P is the pressure (bars), and a is the anhydrous mole
294 fraction of metal oxide components. The values of the model coefficients were identical to those
295 used by Moore et al. (1998), a = 2565, b_{Al2O3} = -1.997, b_{FeOt} = -0.9275, b_{Na2O} = 2.736, c = 1.171,
296 and d = -14.21. Best fit values for water solubility exponents and coefficients were calculated for
297 a pressure of 41 MPa and a temperature of 1700 K. For a very low-Ti picrite, a solubility
298 coefficient of 6.15×10^{-7} and exponent of 0.58914 was obtained, while for a high-Ti/black
299 picrite, a solubility coefficient of 5.69×10^{-7} and exponent of 0.59080 was obtained. For all
300 calculated solubility coefficients and exponents, see Table S2 in Supporting Information.

301   For H_2, solubility parameters σ_{CO} = 3.15×10^{-12} and ϵ_{CO} = 1 were utilised, based on the
302 solubility curves produced by Hirschmann et al. (2012), assuming a lunar mantle oxygen
303 fugacity of IW −1.0. For CO, solubility parameters σ_{CO} = 0.2438×10^{-12} and ϵ_{CO} = 1 were
304 determined using the model by Wetzel et al. (2013), assuming highly reducing conditions in the
305 lunar mantle [Shearer et al., 2006].

306

307   2.4 Equations of State

308   The equations of state describe the internal properties of each phase. For both melt and
309 crystal phases, a linearised version of the Mie-Grüneisen equations of state was adopted [La
310 Spina et al., 2014; La Spina and Michieli Vitturi, 2012]:

311

$$
\begin{cases}
e_k(\rho_k, T) = \bar{e}_k + c_{v,k}T + \dfrac{\rho_{0,k}C_{0,k}^2 - \gamma_k P_{0,k}}{\gamma_k \rho_k}, \\[2mm]
P_k(\rho_k, T) = c_{v,k}(\gamma_k - 1)\rho_k T - \dfrac{\rho_{0,k}C_{0,k}^2 - \gamma_k P_{0,k}}{\gamma_k}, \\[2mm]
s_k(\rho_k, T) = s_{0,k} + c_{v,k}\ln\left[\dfrac{T}{T_{0,k}}\left(\dfrac{\rho_{0,k}}{\rho_k}\right)^{\gamma_k-1}\right], \\[2mm]
C_k(\rho_k, T) = C_{0,k}\sqrt{\left(\dfrac{\rho_k}{\rho_{0,k}}\right)^{\gamma_k-1}\exp\left(\dfrac{s_k(\rho_k, T) - s_{0,k}}{c_{v,k}}\right)},
\end{cases}
\tag{9}
$$

312

313   where k indicates either the melt or crystal phase. Here $\bar{e}_k$ is a constant parameter representing
314 the formation energy of the fluid, $c_{v,k}$ is the specific heat capacity at constant volume, γ_k is the
315 adiabatic exponent, $\rho_{0,k}$, $P_{0,k}$, $T_{0,k}$, $s_{0,k}$ and $C_{0,k}$ are respectively the density, pressure,
316 temperature, specific entropy, and speed of sound at a reference state.

317   For the exsolved gas phase, the Van der Waals equations of state were adopted to take
318 into account the non-ideality of the gas phases [La Spina et al., 2015]:

$$
\begin{cases}
e_{g_i}(\rho_{g_i}, T) = c_{v,g_i}T - a_{g_i}\rho_{g_i} + \bar{e}_{g_i}, \\[2mm]
P_{g_i}(\rho_{g_i}, T) = c_{v,g_i}(\gamma_{g_i} - 1)T\dfrac{\rho_{g_i}}{1 - b_{g_i}\rho_{g_i}} - a_{g_i}\rho_{g_i}^2, \\[2mm]
s_{g_i}(\rho_{g_i}, T) = c_{v,g_i}\log\left[\dfrac{T}{T_{0,g_i}}\left(\dfrac{\rho_{0,g_i}}{\rho_{g_i}}\cdot\left(1 - b_{g_i}\rho_{g_i}\right)\right)^{\left(\gamma_{g_i}-1\right)}\right], \\[2mm]
C_{g_i}(\rho_{g_i}, T) = \sqrt{\dfrac{c_{v,g_i}(\gamma_{g_i} - 1)\gamma_{g_i}T}{\left(1 - b_{g_i}\rho_{g_i}\right)^2} - 2a_{g_i}\rho_{g_i}}
\end{cases}
\tag{10}
$$

319   for $i = 1, \dots, n_g$. The coefficients a_{g_i} and b_{g_i} are defined as

$$
a_{g_i} = \frac{27}{64}\frac{c_{v,g_i}^2(\gamma_{g_i} - 1)^2 T_{c,g_i}^2}{P_{c,g_i}},
\tag{11}
$$

$$
b_{g_i} = \frac{1}{8}\frac{c_{v,g_i}(\gamma_{g_i} - 1)T_{c,g_i}}{P_{c,g_i}},
\tag{12}
$$

320   where P_{c,g_i} and T_{c,g_i} are the critical pressure and temperature of the gas component g_i
321 respectively.

322   2.5 Initial and boundary conditions

323   The initial conditions for our numerical simulations are defined as a set of values for
324 certain parameters at the inlet of the conduit, which were altered between different model runs.
325 The boundary conditions, instead, are the conditions set at the vent of the conduit. For a given
326 combination of initial and boundary conditions, the model calculated all the parameters within

327   the conduit that satisfied those conditions. Specifically, model solutions were obtained using a
328   shooting technique, which consisted of searching for the inlet magma ascent velocity that
329   allowed us to obtain the desired atmospheric pressure or choked flow condition at the conduit
330   outlet [de' Michieli Vitturi et al., 2008]. A choked flow condition is reached when the mixture
331   velocity is equal to the speed of sound in the mixture. To calculate the speed of sound of the
332   mixture, we adopted the equation described in La Spina et al. (2021):

$$C = \frac{1}{\sqrt{K\rho}}, \tag{13}$$

333   where C is the speed of sound in the mixture, $K = \alpha_l K_l + \alpha_g K_g$ is the compressibility of the
334   mixture, and ρ is the density of the mixture.

335   For our investigation on how the magmatic volatile content affects magma ascent
336   dynamics on the Moon, we used the five picritic compositions presented in Table 1. For each
337   model run with these compositions, we assumed a conduit radius of 10 m and a conduit depth of
338   10 km. Compared with larger-scale gravitational anomalies, lunar dykes are difficult to detect
339   and measure using gravimetric data [Andrews-Hanna et al., 2013]. We assumed a conduit radius
340   of 10 m to reflect data from surveys of terrestrial dykes that fed basaltic volcanic systems
341   [Anderson, 1951; Kavanagh and Sparks, 2011; Klausen, 2006]. Although picrites are thought to
342   originate from depths of up to 450 km [Elkins-Tanton et al., 2003b] or ~600 km depth [Brown
343   and Grove, 2015], we only focus on the final 10 km of ascent, where the role of volatile elements
344   in driving magma ascent is more significant and the direct link to eruption conditions is more
345   feasible.

346   We considered the pressure, temperature, H_2, H_2O and CO content, and crystal content as
347   initial conditions at the inlet of the conduit. Values adopted for the model runs are reported in
348   Table 2. Specifically, we set an initial pressure of 41.31 MPa, an initial temperature of 1700 K,
349   and an initial crystal content of 1 vol % (see Text S2 and Datasets S1-2 of Supporting
350   Information) for all model simulations. Regarding the boundary conditions at the conduit outlet,
351   we adopted both a desired pressure at the vent of the conduit and choked flow condition.
352   However, since there is no atmosphere on the Moon, the pressure at the conduit outlet was set to
353   0 Pa. For the volatile contents, we assumed initial H_2O contents between 25 and 1500 ppm,
354   based on reported measurements of lunar glass beads [Saal et al., 2008; Hauri et al., 2011], and
355   equivalent H_2 contents between 2 and 85 ppm, based on molecular weight relative to H_2O.
356   Finally, for CO, we assumed the same initial contents as for H_2O, which matches measurements
357   made by Wetzel et al. (2015) at the lower bound and estimates of the carbon content of the
358   terrestrial mantle at the upper bound [Gerlach et al., 2001] – Table 2.

359

360   Table 2: Initial conditions at conduit inlet used for magma ascent model runs in this study, from
361   values reported in the literature. For the initial crystal content calculations, see Text S2 and
362   Datasets S1-2 of Supporting Information.

Initial condition	Value	Assumptions/Reference
Pressure (Pa)	41310000	Based on a conduit depth of 10 km, an acceleration due to lunar gravity of 1.62 m s^{-2}, and average lunar crustal density of 2550 kg m^{-3} [Wieczorek et al., 2013].

Temperature (K)	1700	Liquidus temperatures of 1673 ± 20 K (green and yellow picritic beads [Fogel and Rutherford, 1995]) and 1623 K (orange picritic beads [Rutherford and Papale, 2009]) have been determined. These values provide a lower bound for this boundary condition.
H_2O content (ppm)	(A) 25 (B) 100 (C) 500 (D) 1000 (E) 1500	Initial H_2O content was varied from 25 ppm, based on measurements ranging from 4 to 46 ppm by Saal et al. (2008), and 1500 ppm, based on measurements of 1410 ppm by Hauri et al. (2011).
H_2 content (ppm)	(a) 2 (b) 6 (c) 28 (d) 56 (e) 85	Equivalent H_2 content obtained from the conversion of H_2O to molecular hydrogen concentrations.
CO content (ppm)	(i) 25 (ii) 100 (iii) 500 (iv) 1000 (v) 1500	The lower limit was based on measurements made by Wetzel et al. (2015), while the upper limit was based on carbon abundances in terrestrial volcanic rocks measured by Hekinian et al. (2000) and Gerlach et al. (2002). The range of initial CO contents were extended to match that of H_2O.
Crystal content (vol %)	1	Initial crystal content of the picritic magma was calculated using MELTS [Ghiorso and Gualda, 2015; Gualda et al., 2012] and did not exceed 1 weight % for any composition of picrite, assuming an initial liquidus temperature for lunar picritic magma of at least 1693 K [Fogel and Rutherford, 1995]. See Text S2 of Supporting Information.

363   2.6 Sensitivity analysis

364   We conducted a sensitivity analysis to determine the relationship between various input
365   parameters (inlet temperature and pressure, H_2 content, H_2O content, CO content, and conduit
366   radius) and model outputs for quantities within the conduit (gas volume fraction, exit pressure,
367   exit velocity, and mass flow rate). The sensitivity analysis was performed using the Dakota
368   toolkit [Adams et al., 2019], which is an open-source software produced by Sandia National
369   Laboratories. The software has a broad range of uses including model calibration, risk analyses,
370   and uncertainty quantification. For our sensitivity analyses, we adopted a Latin hypercube
371   sampling technique to vary the different input parameters within set ranges, in a more efficient
372   manner than random sampling [Iman and Conover, 1980; McKay et al., 1979]. We performed a
373   sensitivity analysis with H_2O and CO using 10,000 different model simulations for each of the
374   five magma compositions (Table 1), varying the combination of input parameters with a uniform
375   distribution within the ranges considered. An additional sensitivity analysis using H_2 and CO as
376   volatile species for an intermediate-Ti picrite was also performed to compare the results with the
377   corresponding H_2O-CO case. Specifically, the initial temperature was varied between 1600 K
378   and 1800 K, the inlet pressure between 40 MPa and 45 MPa, the H_2O and CO content between 5

379 ppm and 1500 ppm, the H_2 content between 2 ppm and 90 ppm, and the conduit radius between
380 10 m and 100 m – see Table S3 of Supporting Information for full information.

381   We chose to analyse four model outputs: gas volume fraction, exit pressure, exit velocity,
382 and mass flow rate. These model outputs have a direct control on many aspects of eruptive
383 behaviour, such as the ejection distance of pyroclastic material, the height of an eruption plume,
384 and the overall style of the volcanic eruption [Sigurdsson, 2015; Wilson, 1972; Wilson, 1980].

385

3 Results

386

387   3.1 Model outputs

388   We present numerical results for (i) the H_2O and CO model simulations and (ii) the H_2
389 and CO model simulations. For the H_2O and CO model simulations, we present results for the
390 two end-member compositions of picrite: green/very low-TiO_2 (VLT) glass (Fig. 1), and
391 black/high-TiO_2 glass (Fig. 2). In both Figs. 1 and 2 we plot the numerical results obtained with a
392 lower volatile content (i.e., 25 ppm of H_2O and 25 ppm of CO, blue lines) and with a higher
393 volatile content (i.e., 1500 ppm of H_2O and 1500 ppm of CO, red lines). For the H_2 and CO
394 model simulations, we present results for a green/VLT picrite with a lower bound volatile
395 content of 2 ppm H_2 and 25 ppm CO and an upper bound volatile content of 84 ppm H_2 and 1500
396 ppm CO (Fig. 3). There was little variation in the results between the five end-member
397 compositions of picrite, for both the H_2O and CO and the H_2 and CO model simulations,
398 therefore, we have chosen to present results from only one or two compositions below. For
399 model results for all five magma compositions, see Figs. S1 to S15 of the Supporting
400 Information.

401   The model results presented for H_2O and CO simulations in Figs. 1a-b, 2a-b, and 3a-b
402 show a continuous decrease in pressure and temperature for the majority of the conduit. For the
403 lower initial volatile content simulation, an exit pressure of 0.05 MPa was reached, while an exit
404 pressure of 0.6 MPa was reached for the higher initial volatile content simulation. Calculated exit
405 pressure was always greater than zero (the surface pressure on the Moon) so for all simulations
406 the model reached the choked-flow condition at the vent of the conduit.

407   For the temperature (Figs. 1b, 2b, and 3b), we saw a constant cooling of 10-15 °C after
408 10 km of ascent. The temperature gradient from the conduit inlet to the surface was relatively
409 low compared to terrestrial low viscosity basaltic magmas [La Spina et al., 2015, 2017, 2021] for
410 two main reasons. First of all, the crystal content was fixed at 1 vol %, therefore, there was no
411 latent heat of crystallisation being released into the system [Blundy et al., 2006; La Spina et al.,
412 2015]. Secondly, the volatile content in most of the model simulations was very low (<0.15 wt.%
413 in total), meaning that there would be little expansion of bubbles during ascent, which limits
414 adiabatic cooling [Kavanagh & Sparks, 2009; La Spina et al., 2015].

415   For the H_2O and CO model simulations, mixture velocity, gas-melt slip velocity, and
416 viscosity were constant for the majority of the conduit, with changes only occurring within the
417 final 2 km or less of ascent (Figs.1c-e and 2c-e). During ascent, mixture velocity was almost
418 constant. From a depth of 10 km to 1km, a mixture velocity of ~6 m s^{-1} was calculated for the
419 low volatile content simulations, and a mixture velocity of ~8 m s^{-1} was calculated for the high
420 volatile content simulations. From 1 km to the surface, the magma accelerated, with the mixture

421   velocity reaching values of ~10 m s^{-1} (simulations with lower initial volatile contents) to 40 m s^{-1}
422   (simulations with higher initial volatile content). Mixture velocity did not vary significantly
423   across the different compositions. The near constant mixture velocity reflects the low volatile
424   content assumed for the simulated magmas. Indeed, even the higher volatile content simulations
425   do not contain sufficient exsolved volatiles to affect magma buoyancy for most of the conduit,
426   and therefore ascent at depth would be mainly driven by the pressure gradient. It should be noted
427   that these results only represent processes occurring within the conduit, so the ejection velocities
428   are likely to be greater than those reported here, due to the further expansion and acceleration
429   that the magma would experience upon exiting the vent. Gas-melt slip velocity was basically
430   zero from the conduit inlet to the surface for the low volatile content simulations, which means
431   that the bubbles would stay coupled with the melt during ascent, i.e. outgassing would be mostly
432   inhibited. For the high volatile content simulations, it appears that bubbles started to decouple
433   from the melt at a depth of ~ 4 km, however, this does not appear to have affected the overall
434   magma ascent dynamics significantly (Figs. 1d and 2d). For the H_2 and CO model simulations,
435   the bubbles appear to begin to decouple from the melt at a greater depth of ~ 6 km (Fig. 3d).

436   The calculated viscosity of the magma was very low compared to terrestrial simulations
437   for all model simulations, with values of approximately 0.5-5 Pa s for the very low-TiO_2/green
438   picritic magma, and approximately 10-30 Pa s for the high-TiO_2/black picritic magma. This is
439   likely a result of the low silica content of picrites, high source temperature and very low crystal
440   content, which reduces the viscosity of the melt. This result is consistent with viscosity values
441   reported by Williams et al. (2000).

442   We can see that fragmentation was not expected to occur within the conduit as the critical
443   Deborah number (black lines on Figs. 1f, 2f, and 3f) needed to trigger fragmentation [Papale,
444   1999] was not exceeded. However, the rapid decompression and expansion expected once
445   magma is ejected from the vent due to the negligible pressure outside the conduit would likely
446   trigger inertial or fluid-dynamic fragmentation [Jones et al., 2019, La Spina et al., 2021; Namiki
447   and Manga, 2008]. This suggests that the magma would fragment upon reaching the surface,
448   producing a lava fountaining style [La Spina et al., 2021], which is consistent with many models
449   presented previously [Carter et al., 2009; Coombs and Hawke, 1992; Elkins-Tanton et al., 2003a;
450   Fogel and Rutherford, 1995; Weitz et al., 1998].

451   Finally, our results show that for the range of H_2O and CO contents and compositions
452   modelled here, the calculated mass flow rate was always between 3.4×10^6 and 6.7×10^6 kg s^{-1}.
453   For the H_2 and CO model simulations, the mass flow rate showed similar values, ranging from
454   4.4×10^6 and 8.0×10^6 kg s^{-1} (see Table S4 of Supporting Information for full results and details
455   of all model simulations). The slightly lower solubility of H_2 compared with H_2O and its
456   behaviour of exsolving at greater depth result in a more buoyant magma. However, the results
457   for the H_2O and CO model simulations do not differ greatly from the results of the H_2 and CO
458   model simulations. The main differences are in the gas-slip velocity and the mass flow rate,
459   differences that both appear to stem from the slightly lower solubility of H_2 in magma compared
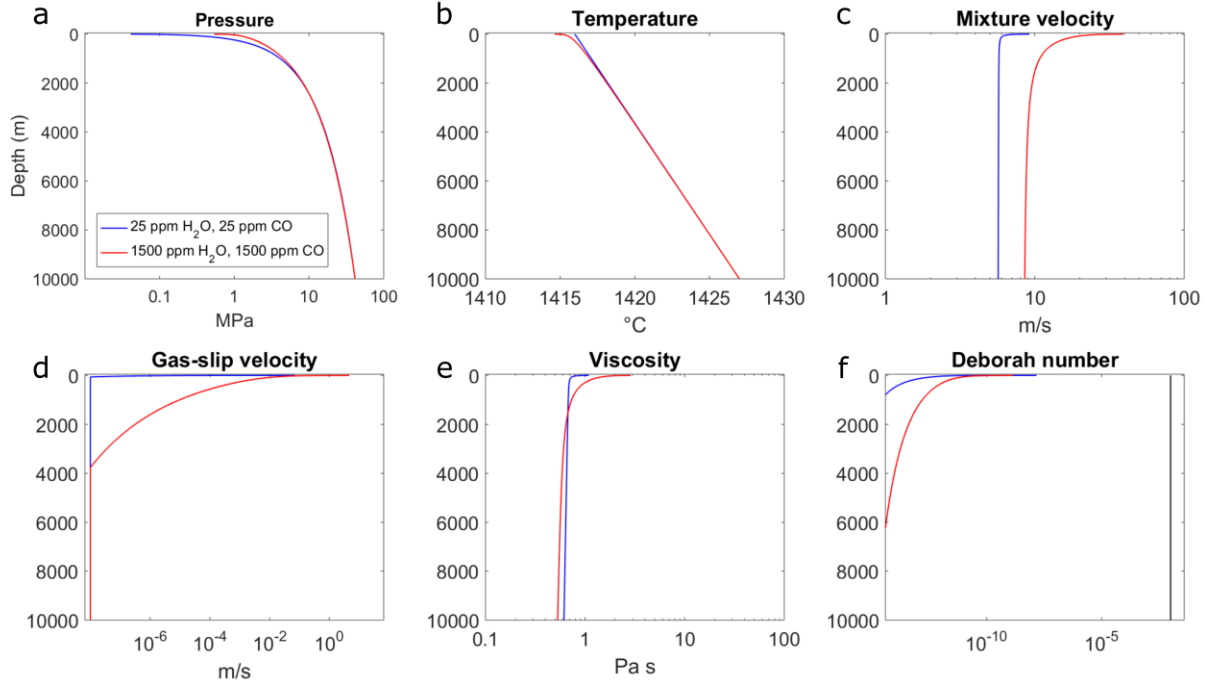460   with H_2O.
461
462

Figure 1: Numerical results for a green/VLT picrite with an initial volatile content of 25 ppm H_2O and 25 ppm CO (blue curve) and 1500 ppm H_2O and 1500 ppm CO (red curve): (a) pressure, (b) temperature, (c) mixture velocity, (d) gas/melt relative velocity, (e) mixture viscosity, and (f) Deborah number. The black line in panel (f) represents the critical Deborah number above which fragmentation is triggered.
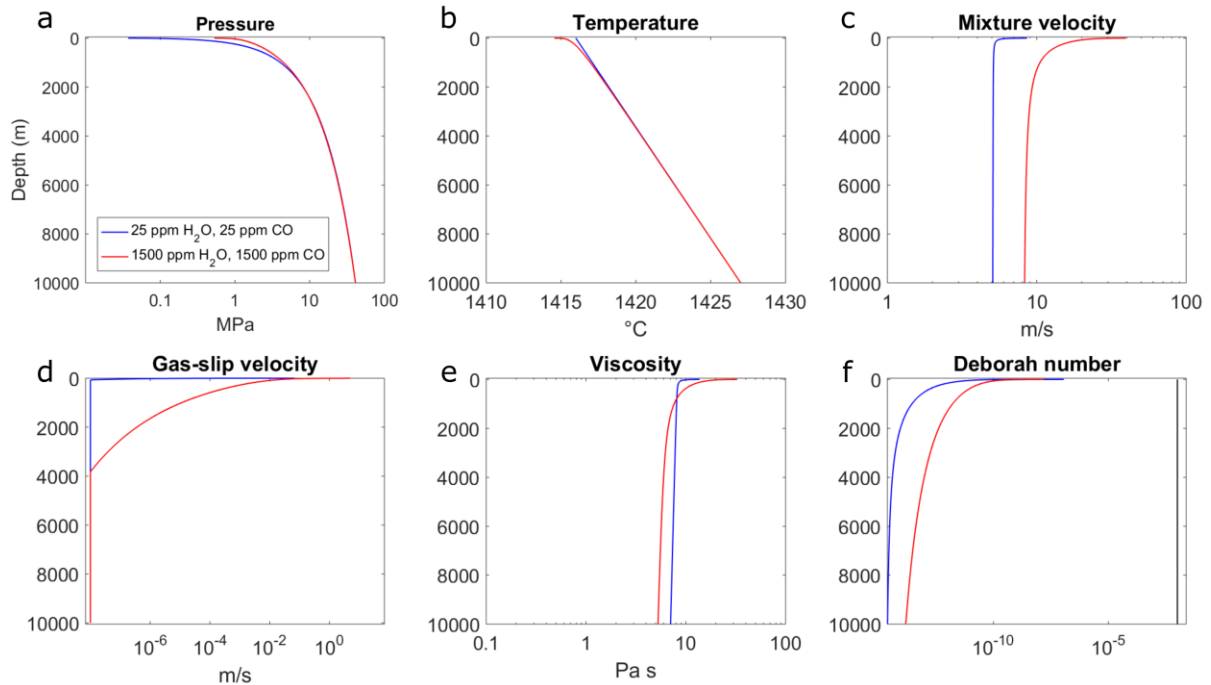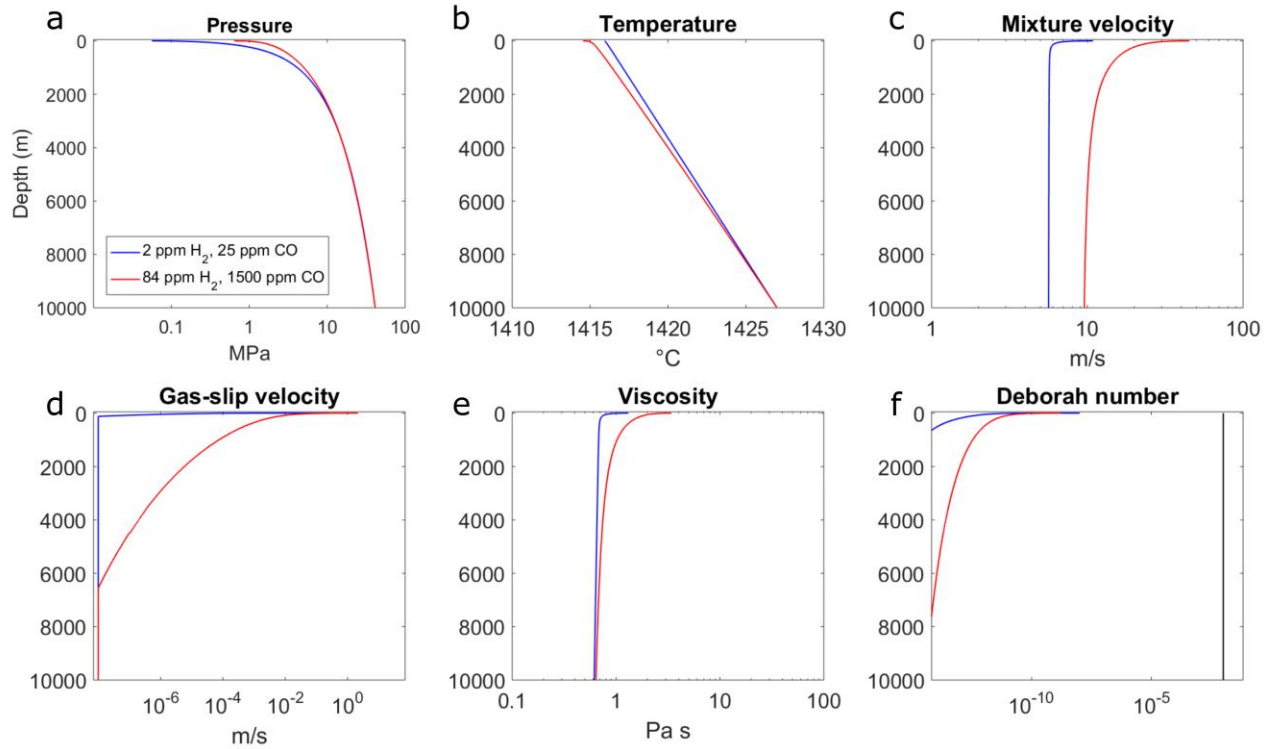

Figure 2: Numerical results for a black/high-Ti picrite with an initial volatile content of 25 ppm H_2O and 25 ppm CO (blue curve) and 1500 ppm H_2O and 1500 ppm CO (red curve): (a)

474 pressure, (b) temperature, (c) mixture velocity, (d) gas/melt relative velocity, (e) mixture
475 viscosity, and (f) Deborah number. The black line in panel (f) represents the critical Deborah
476 number above which fragmentation is triggered.
477
478

479
480 Figure 3: Numerical results for a green/VLT picrite with an initial volatile content of 2 ppm H_2
481 and 25 ppm CO (blue curve) and 84 ppm H_2 and 1500 ppm CO (red curve): (a) pressure, (b)
482 temperature, (c) mixture velocity, (d) gas/melt relative velocity, (e) mixture viscosity, and (f)
483 Deborah number. The black line in panel (f) represents the critical Deborah number above which
484 fragmentation is triggered.
485
486

487   3.2 Volatile exsolution during ascent

488   We now analyse the effect of the different initial volatile contents assumed on the
489 exsolution of volatiles during ascent and on the resulting gas volume fractions. We present
490 results for a yellow/intermediate-Ti picrite from 10 km (Fig. 4) and 2 km (Fig. 5) depth to the
491 surface. For the model simulations concerning H_2O and CO, Figs. 4a and 5a show that, for range
492 of magma compositions and initial magmatic volatile contents modelled, CO made up the
493 majority of the volume fraction of exsolved gas. For the low volatile content simulations, the
494 total volume fraction of exsolved gas reaches 0.4 (Figs. 4a and 5a, red dashed line), 70-75% of
495 which is CO. For the higher volatile content simulations, instead, the total exsolved gas volume
496 fraction reaches 0.8 (Figs. 4a and 5a, red solid line) at the vent of the conduit, 50-55% of which
497 is CO. However, for most part of the conduit, CO is the dominant volatile species. These results
498 are likely a product of the higher solubility of H_2O in magma compared to CO.

499   Results show that the amount of H_2O dissolved within the magma remains constant,
500   except for when the high volatile content simulation reaches the upper 250 m of the conduit (Fig.
501   4b). Meanwhile, most of the CO is already exsolved at 10 km depth, with only a small amount
502   left dissolved in the melt (Fig. 4c). This is a result of the low solubility of CO in lunar magmas.
503   However, due to the high pressure, the exsolved CO volume fraction remains small until shallow
504   depths (see green curves on Figs. 4a and 5a).
505   The depth at which H_2O and CO exsolved showed little variation from very low- to high-
506   Ti magma (Figs. S1 to S15 of Supporting Information); it appears that the magma compositions
507   investigated here have little effect on the volume fraction of exsolved gas during ascent. The
508   variation in major element composition does not seem to affect the solubility of the volatiles in
509   the magma to a significant degree.
510   For the H_2 and CO model simulations, the role of both volatiles in driving magma ascent
511   seems comparable, with H_2 being slightly more dominant for the low volatile content simulations
512   (Fig. 4d and 5b). Fig. 4d shows that, for the low volatile content simulations, H_2 makes up 65-
513   70% of the total volume fraction of exsolved gas (0.5). For the high volatile content simulations,
514   H_2 makes up 55-60% of the total volume fraction of exsolved gas (0.8).
515   H_2 appears to be slightly less soluble in magma than H_2O, with H_2 exsolving more
516   gradually between 10 and 2 km depth, compared with the more rapid exsolution of H_2O at
517   shallow depths of 1-2 km (Figs. 4b and 4d). Overall, these results show that, for the range of
518   volatiles and volatile contents considered here, the dominant volatile that makes up the majority
519   of the exsolved gas fraction is depending on which H-species is initially selected, giving a strong
520   dependence on factors such as the oxygen fugacity of the system.
521

522
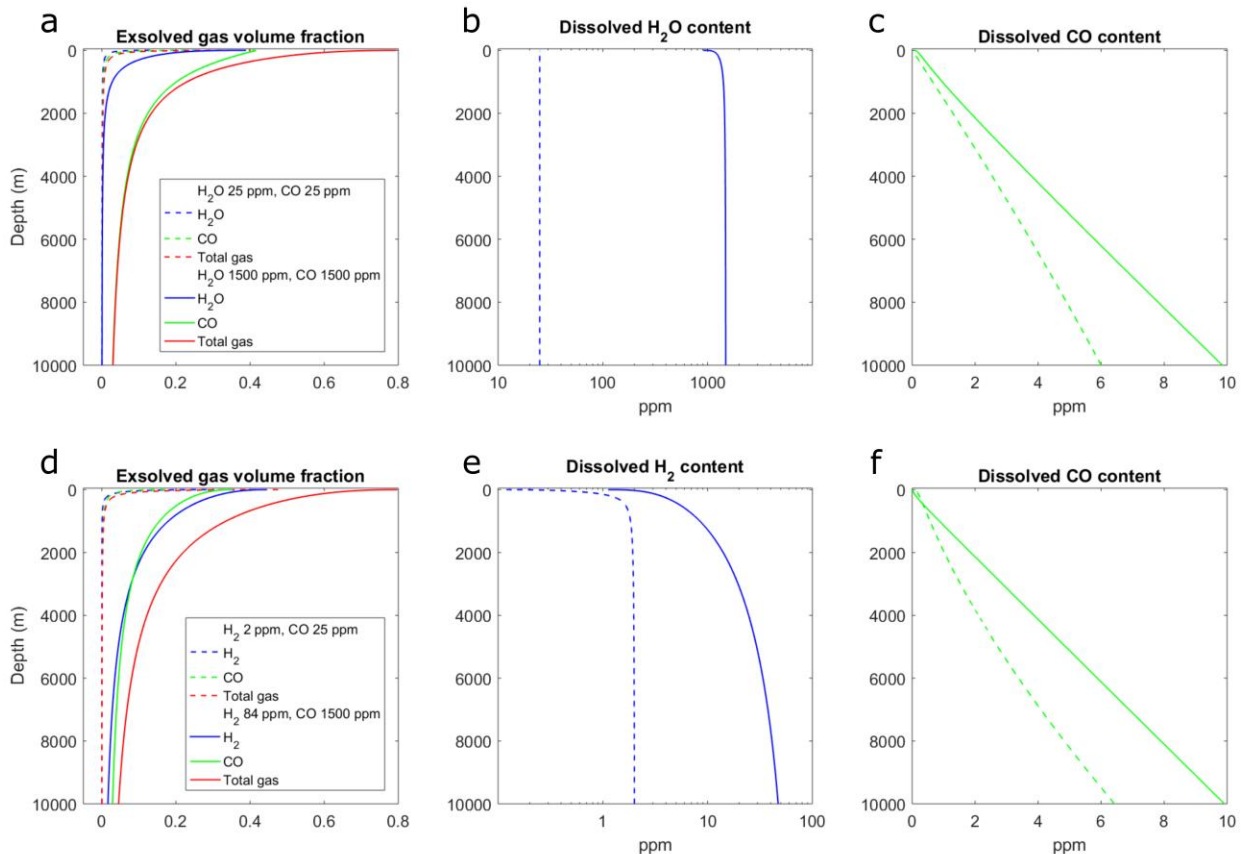
Figure 4: Volume fraction of exsolved gas and dissolved H_2O/H_2 and CO plots for a yellow/intermediate-Ti magma containing H_2O and CO (panels a-c) and H_2 and CO (panels d-f), all from a depth of 10 km to the surface. Dashed lines represent an initial volatile content of 25 ppm H_2O and 25 ppm CO, or 2 ppm H_2 and 25 ppm CO. Solid lines represent an initial volatile content of 1500 ppm H_2O and 1500 ppm CO, or 84 ppm H_2 and 1500 ppm CO. Red lines represent the total volatile content, blue lines represent the H_2O or H_2 amount, and green lines represent the CO amount.
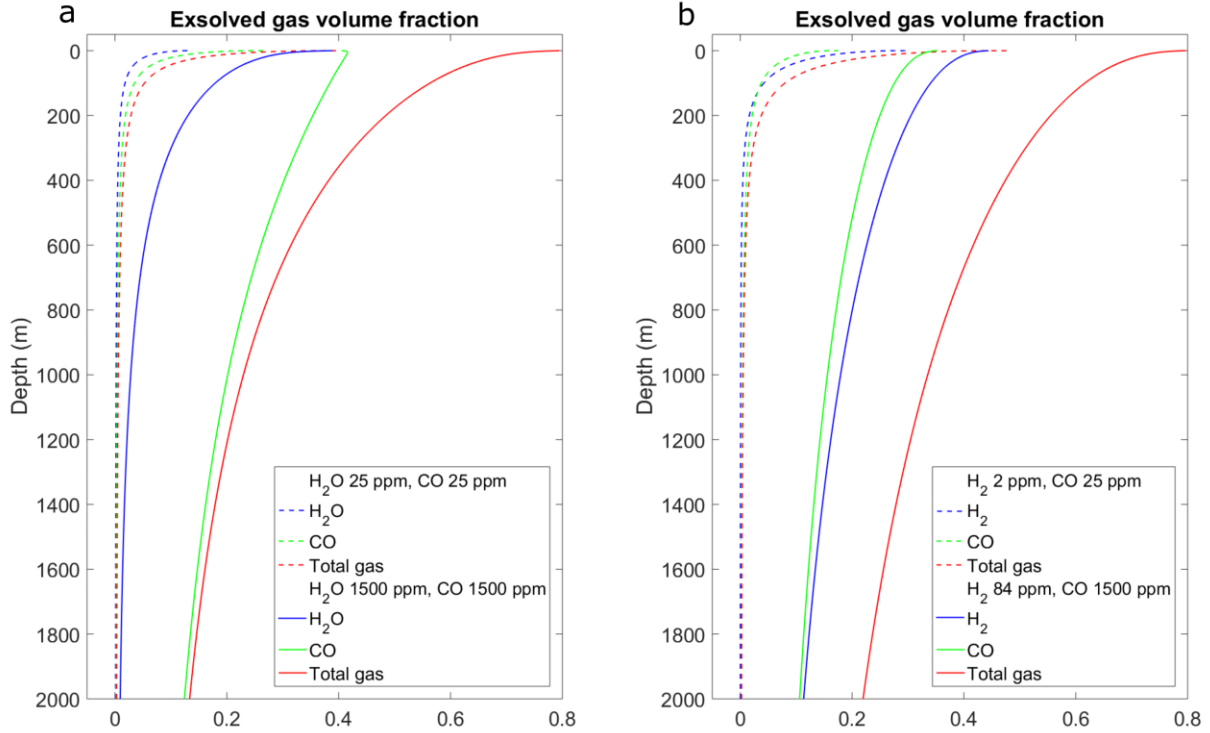
Figure 5: Volume fraction of exsolved gas and dissolved H_2O/H_2 and CO plots for a yellow/intermediate-Ti magma containing H_2O and CO (panel a) and H_2 and CO (panel b), from a depth of 2 km to the surface. Dashed lines represent an initial volatile content of 25 ppm H_2O and 25 ppm CO, or 2 ppm H_2 and 25 ppm CO. Solid lines represent an initial volatile content of 1500 ppm H_2O and 1500 ppm CO, or 84 ppm H_2 and 1500 ppm CO. Red lines represent the total volatile content, blue lines represent the H_2O or H_2 amount, and green lines represent the CO amount.

3.3 Sensitivity analysis

The results of the sensitivity analysis for the have been illustrated with: plots showing frequency against selected output parameters (Figs. 6 and 7); Sobol index plots (Fig. 8); and correlation plots showing the relation between each volatile component against both exit velocity and exit pressure (Figs. 9 and 10). The Sobol index of a given output parameter is a measure of how the variability in the output value is linked to the variability of different model inputs (La Spina et al., 2019). Therefore, the Sobol index can be used to comment on the relative influence of one input parameter (within the ranges investigated in the sensitivity analysis) on a specific

548 output. The model inputs we analysed were: pressure, temperature, conduit radius, H_2O or H_2
549 content, and CO content. The four model outputs we focus on are: exit gas volume fraction, mass
550 flow rate, exit velocity, and exit pressure. We focus on results for a yellow/intermediate-Ti
551 picrite for both the H_2 and CO and the H_2O and CO model simulations. For sensitivity analysis
552 results for all picrite compositions, see Figs. S16 to S27 in Supporting Information.

553   Our results show that both mixtures of volatiles (H_2O-CO, and H_2-CO) produce a very
554 similar exit gas volume fraction, mass flow rate, exit velocity, and exit pressure (Figs. 6 and 7,
555 Table 3). The only notable difference is that each of these model output parameters were
556 consistently higher for the H_2-CO mixture, compared with the model simulations obtained
557 assuming a H_2O-CO gas mixture by roughly 5-10 %.

558   The Sobol index plots (Fig. 8) indicate that exit gas volume fraction was affected by all
559 five input parameters tested. For the H_2O-CO model simulations, H_2O had a lower effect than
560 that of CO. For the H_2-CO model simulations, instead, H_2 played a larger role than CO in
561 affecting the gas volume fraction at the vent of the conduit. For both combinations of volatiles,
562 mass flow rate was majorly controlled by conduit radius. For the H_2O-CO model simulations,
563 CO was the dominant input parameter for controlling both exit velocity and exit pressure, with
564 minimal contribution from H_2O. However, for the H_2-CO model simulations, H_2 and CO were
565 roughly equal in terms of controlling the model output.

566   The significance of CO compared with H_2O can be seen in the correlation plots for exit
567 velocity and pressure (Fig. 9). These are illustrated in Fig. 9 where each red point is the output
568 value resulting from one simulation, whereas the blue line is the mean value of the outputs
569 obtained for the given value of the corresponding input parameter. The higher the gradient of the
570 blue line, the more significant the input parameter is for controlling the output. The blue lines for
571 H_2O content are almost flat (Figs. 9a and 9c), indicating that, across the H_2O contents
572 investigated in the sensitivity analysis, H_2O is not affecting the exit velocity and exit pressure,
573 confirming the findings of the Sobol index results. On the contrary, the gradient of the CO
574 content curves is greater than that for H_2O, which indicates that CO has a greater influence on
575 the calculated exit velocity and pressure (Figs. 9b and 9d). This is likely to be a consequence of
576 the relatively low initial H_2O content assumed and of the higher solubility of H_2O in magma
577 compared to CO. Indeed, the combination of both results is an exsolution of H_2O only at very
578 shallow depth, and thus water is not able to affect significantly the magma ascent dynamics. In
579 Fig. 10, we see that the gradient between H_2 and CO and exit velocity and exit pressure are very
580 similar, suggesting that they have an equal effect on magma ascent dynamics.
581
582
583 Table 3: Summary of the frequency against selected output parameters graphs (Figs. 6 and 7).

| Output		H_2O and CO	H_2 and CO
Gas Volume Fraction	Range	0.05-0.95	0.20-0.95
	Peak	0.45-0.55	0.55-0.65
Mass flow rate (log 10 kg s$^{-1)}$	Range	5.6-9.4	6.0-9.4
	Peak	8.5-9.0	8.8-9.2
Exit Velocity (m s^{-1})	Range	6-60	8-67
	Peak	35-40	40-45
Exit pressure (log Pa)	Range	3.3-6.2	3.5-6.3
	Peak	5.7-6.0	5.9-6.1

584

585

586

587
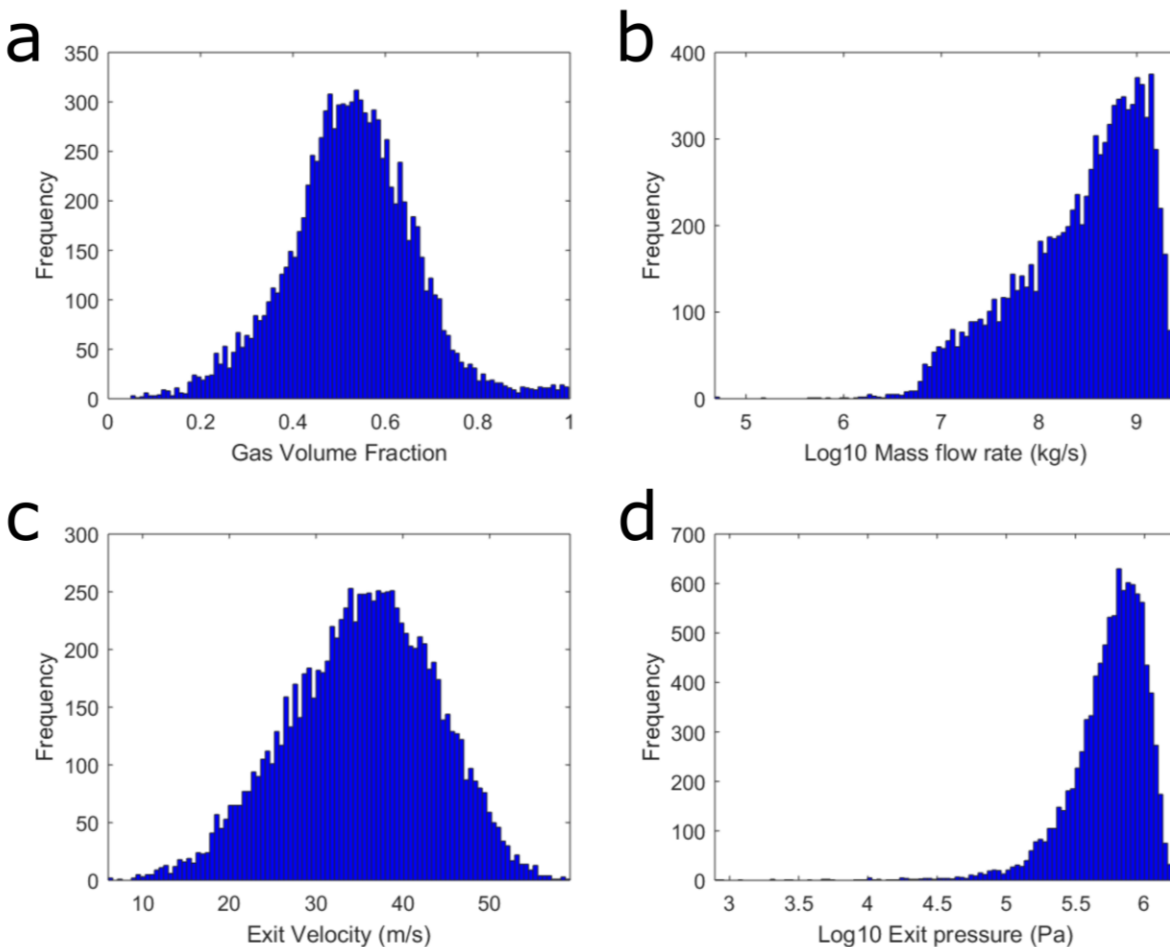
588 Figure 6: Frequency against selected output parameters obtained from the sensitivity analysis
589 assuming a yellow/intermediate-Ti magma containing H_2O and CO: (a) exit gas volume fraction,
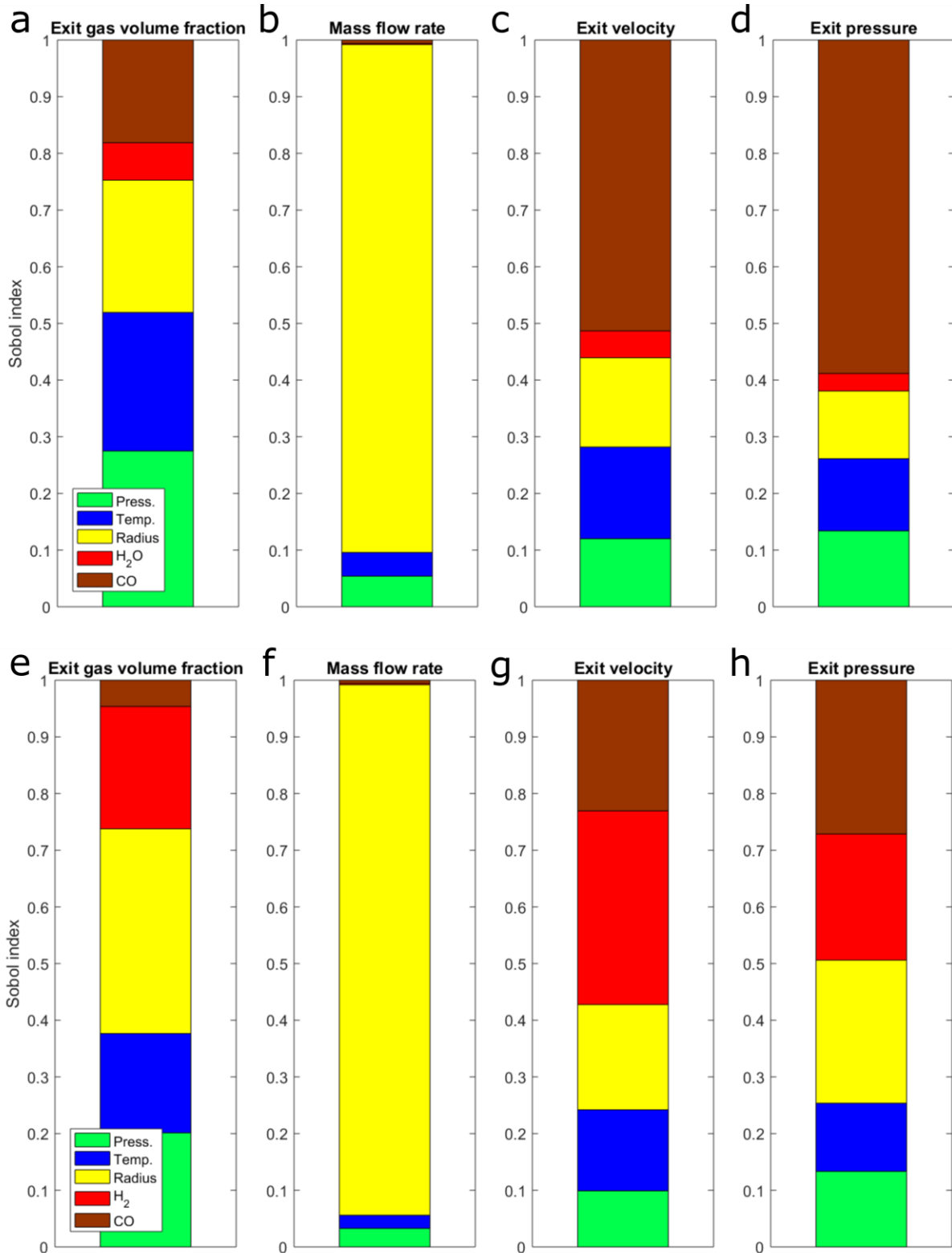590 (b) mass flow rate, (c) exit velocity, and (d) exit pressure.

591
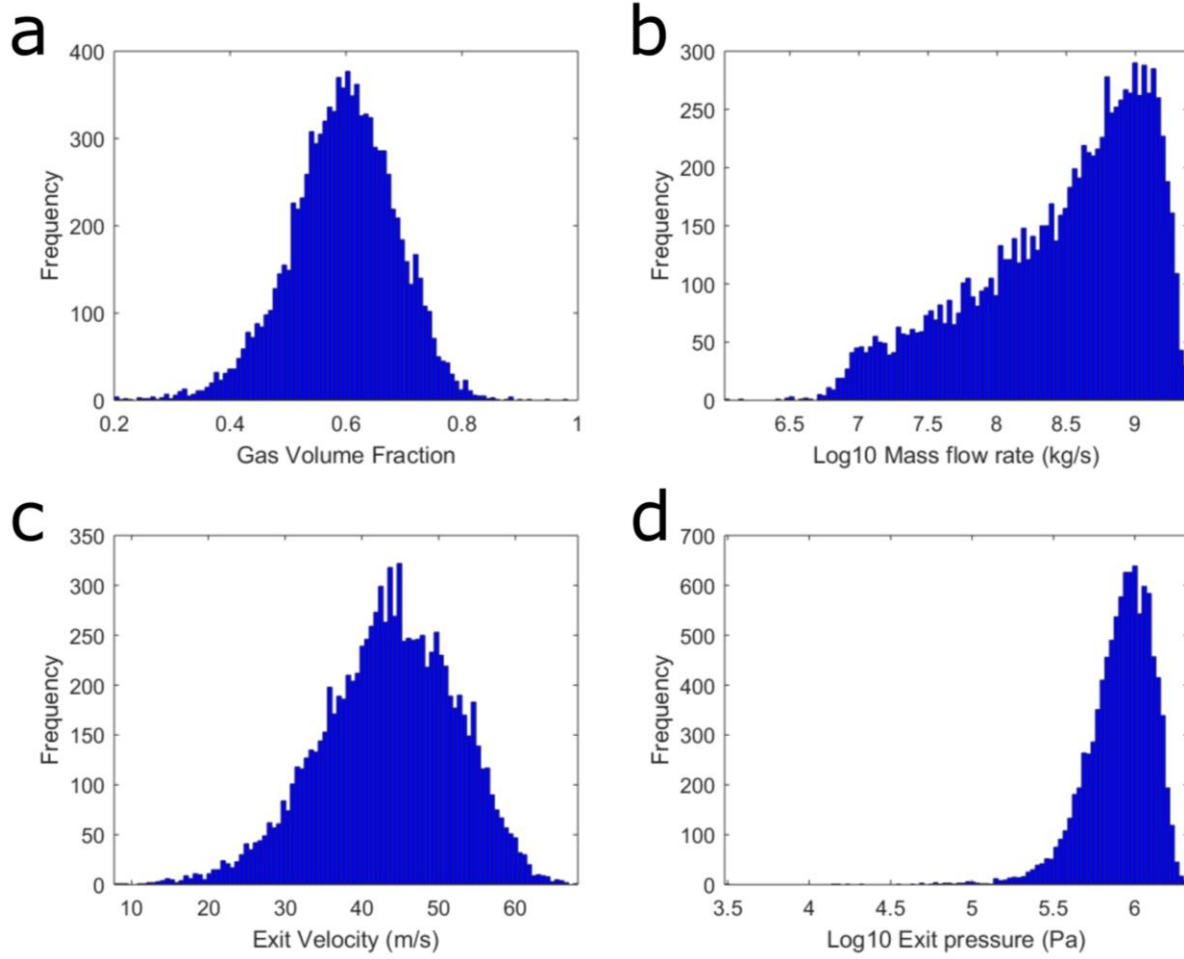
Figure 7: Frequency against selected output parameters obtained from the sensitivity analysis assuming a yellow/intermediate-Ti magma containing H_2 and CO: (a) exit gas volume fraction, (b) mass flow rate, (c) exit velocity, and (d) exit pressure.

Figure 8: Sobol index plot obtained from the sensitivity analysis for yellow/intermediate-Ti magma containing H_2O and CO (panels a-d) and H_2 and CO (panels e-h), showing the relative important of pressure, temperature, conduit radius, initial H_2O content, and initial CO content on

599   exit gas volume fraction (panels a and e), mass flow rate (panels b and f), exit velocity (panels c
600   and g), and exit pressure (panels d and h). Results are based on 10,000 model simulations.

601

602
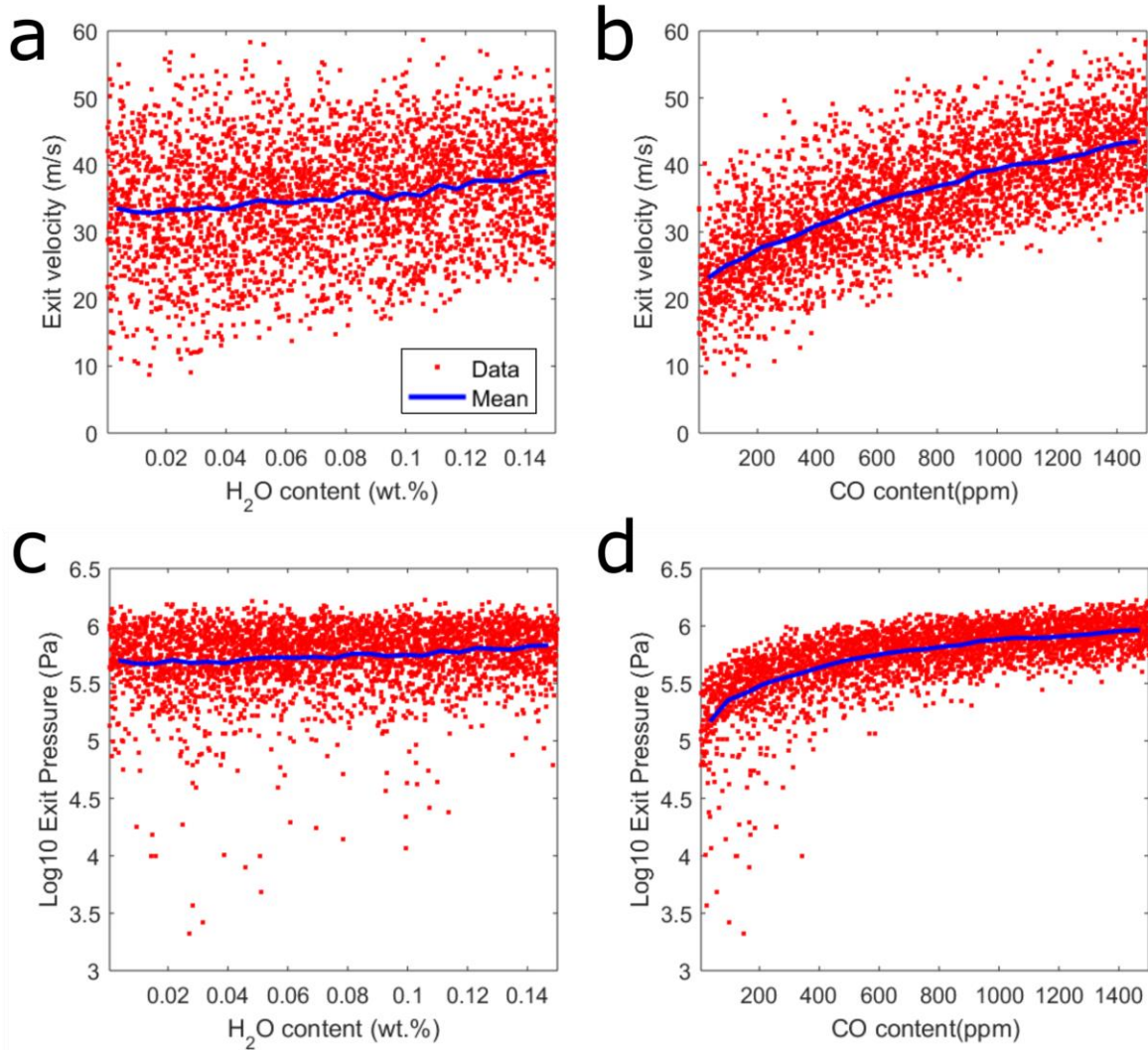
603   Figure 9: Correlation plots obtained from the sensitivity analysis for a yellow/intermediate-Ti
604   picrite containing H_2O and CO, showing the variability of: exit velocity as function of (a) H_2O
605   content, and (b) CO content; and exit pressure as function of (c) H_2O content, and (d) CO
606   content. Each red point represents 1 of the 10,000 simulations. Each blue line represents the
607   mean output value calculated for a given value of the input parameter. The gradient of each blue
608   line indicates how strongly the input parameter affects the corresponding output parameter.

609

Figure 10: Correlation plots obtained from the sensitivity analysis for a yellow/intermediate-Ti picrite containing H_2 and CO, showing the variability of: exit velocity as function of (a) H_2 content, and (b) CO content; and exit pressure as function of (c) H_2 content, and (d) CO content. Each red point represents 1 of the 10,000 simulations. Each blue line represents the mean output value calculated for a given value of the input parameter. The gradient of each blue line indicates how strongly the input parameter affects the corresponding output parameter.

4 Discussion

4.1 Importance of volatile content and composition on magma ascent dynamics on the Moon

622   Our numerical modelling and sensitivity analysis results have shown that for a magma
623   containing H_2O and CO, CO has a stronger control on lunar magma ascent dynamics than H_2O,
624   for the range of initial volatile contents we investigated. Conversely, we have also shown that for
625   a magma containing H_2 and CO, H_2 has a comparable or slightly stronger control on lunar
626   magma ascent dynamics than CO.

627   According to our sensitivity analysis, for a magma containing H_2O and CO, initial CO
628   content was the most significant input parameter controlling exit velocity and exit pressure (Fig.
629   8), out of the input parameters analysed. Initial CO content was also more significant than initial
630   H_2O content for controlling the exsolved gas volume fraction, although initial pressure and
631   temperature had a greater contribution than each of the volatiles. This result is in agreement with
632   several previous studies that state that CO was a key volatile in driving lunar magma ascent and
633   eruptions [Rutherford et al., 2017; Rutherford and Papale, 2009; Sato, 1979; Spera, 1992; Wilson
634   and Head, 2017]. For the simulated magma containing H_2 and CO, the sensitivity analysis results
635   showed that H_2 content had a greater or roughly the same effect as CO content on the exit gas
636   volume fraction, pressure, and velocity. Again, this is in agreement with recent studies that have
637   considered H_2 to be a key volatile element in driving lunar magma ascent [McCubbin et al.,
638   2015], although traces of H_2 have not yet been detected in the volatile-rich coatings on
639   pyroclastic beads.

640   Since the initial CO and H_2 content of a magma (containing H_2O and CO or H_2 and CO
641   respectively) has a strong control on the exit pressure and exit velocity, the initial CO or H_2
642   content must also have a significant degree of control on the shape of an eruption plume,
643   eruption plume size, and the distances that pyroclasts would be ejected. With a greater exit gas
644   volume fraction and exit pressure, we would expect that the later expansion of the eruption
645   plume would be greater. According to Head and Wilson (2017), lunar volcanic plumes are made
646   of a gas cloud, which expands hemispherically, and pyroclasts decoupled from the gas cloud,
647   which disperse following ballistic trajectories. The wide angle expansion of the gas cloud is a
648   result of gas expansion in a vacuum. Furthermore, as the gas expands its density continues to
649   decrease, until it is so small that the drag force on the pyroclasts becomes negligible (the critical
650   gas density), and thus they decouple from the gas cloud following mainly ballistic trajectories. If
651   a significant proportion of the pyroclasts are following a ballistic trajectory, a radial dispersal
652   would be observed, ultimately creating a thin and widely dispersed pyroclastic deposit. However,
653   before the critical gas density is reached, pyroclasts are affected by gas cloud expansion, and
654   they are accelerated reaching velocities of several hundred of meters per second. The exit
655   pressure and gas volume fraction at the vent of the conduit will affect the expansion of the gas
656   cloud and the reaching of the critical gas density, influencing the pyroclasts ejection velocities,
657   and ultimately the deposit.

658   Regarding magma fragmentation during ascent, our numerical results suggest that
659   fragmentation would not occur within the conduit. The low and high volatile content simulations
660   produced a similar Deborah number (approximately 10^{-7}), which was too low to reach the
661   fragmentation threshold. Brittle or inertial fragmentation are likely to occur once magma is
662   ejected from the vent, due to the strong acceleration that the magma will experience following
663   the expansion of the gas cloud in the lunar vacuum. Which one of the two competing
664   mechanisms is more likely to take place is difficult to forecast with our current numerical tool,
665   and more appropriate modelling of this process is required. This would be also important to
666   elucidate the role of the initial volatile content on magma fragmentation within a gas cloud. The

667 link between initial volatile content and pyroclastic deposit morphology has recently been
668 explored by Morgan et al. (2021), using measurements of volatile abundance and release patterns
669 from experiments to estimate pyroclast grain size distributions and their subsequent ejection
670 distances. Their results predicted a bimodal pyroclastic grain size distribution, a maximum
671 pyroclast ejection distance of 20 km (a distance that encompasses 79% of all observed lunar
672 pyroclastic deposits), and that a wide range of volatile contents are responsible for producing the
673 wide range of deposit sizes observed. Future developments could involve utilising the magma
674 ascent model results in the context of the Morgan et al. (2021) work.

675 We can also comment on the effect of different compositions on magma ascent dynamics,
676 since we modelled the full range of picritic compositions from a green/very low-Ti to a
677 black/high-Ti picrite. The magmatic major element compositions investigated here seem to not
678 have a significant effect on the overall magma ascent dynamics. As expected, the only parameter
679 that appears to be affected by magma composition is viscosity, with an order of magnitude
680 difference between the green/VLT picrite (viscosity of ~1 Pa s) to the black/high-Ti picrite
681 (viscosity of ~10 Pa s). This variation in viscosity is not enough to produce a significant effect on
682 magma ascent dynamics and, thus, the simulations obtained with the different compositions are
683 very similar to one another (Figs. 1 and 2).

684 It is important to highlight that we have tested a range of initial volatile contents based on
685 measurements and modelled values from returned samples of lunar picritic glass beads [Saal et
686 al., 2008; Wetzel et al., 2015], supplemented by data from terrestrial volcanic systems where
687 there is limited data on lunar volcanic systems [Gerlach et al., 2002; Hekinian et al., 2000].
688 Therefore, any errors or uncertainties associated with these measurements are carried forward to
689 our results.

690 Finally, we modelled the ascent of a magma containing combinations of H_2 and CO (to
691 represent the most likely H- and C-species, based on geochemical conditions present in the lunar
692 mantle) and H_2O and CO (to utilise the plethora of information available on the behaviour of
693 H_2O in silicate melts). The results of the two different modelling scenarios show opposing results
694 in terms of whether an H- or C-species is dominating magma ascent and eruption dynamics. We
695 cannot be sure which of the two different modelling scenarios are more accurate, since the exact
696 proportions in which H would partition into H_2O and H_2 at 10 km depth within the lunar mantle
697 are not fully understood. Renggli et al. (2017) highlighted the importance of redox conditions in
698 controlling H speciation, while Hirschmann et al. (2012) also demonstrated the importance of
699 pressure and magmatic H_2 content on H speciation. Hirschmann et al. (2012) calculated that, for
700 a magma containing 1000 ppm H_2 at a pressure of 0.1 GPa (i.e., conditions on the same order of
701 magnitude as this study), the molar ratio of H_2 within a magma would be 10-30%. The molar
702 ratio of H_2 within a melt only exceeds 50% for a magma containing >2000 ppm H_2 at >3 GPa,
703 suggesting that, for the pressure conditions simulated in this study, H_2O would be the dominant
704 H-species in the magma. Overall, the results from this study highlight the importance of factors
705 such as melt system oxygen fugacity, H content, and pressure in understanding how H partitions
706 between H_2O and H_2 in magmas, and, therefore, how different volatile elements control magma
707 ascent and eruption.

708 4.2 Comparison with results from previous magma ascent models and experiments

709 We compare our findings with results from previous numerical and experimental models
710 [Rutherford et al., 2017; Rutherford and Papale, 2009; Wilson and Head, 2018]. Our sensitivity

711 analysis showed that, across all initial volatile contents and compositions, exit mixture velocity
712 varied from 5 to 60 m s^{-1}, with a peak in the middle of this range at 25 to 35 m s^{-1}. These results
713 match previous estimates for average ascent velocity of 20 to 30 m s^{-1} [Wilson and Head, 2018],
714 and previous estimates for exit mixture velocity between 15 to 35 m s^{-1} [Rutherford and Papale,
715 2009]. This is useful for understanding the conditions and style with which the picritic glass
716 beads erupted, such as eruption height and pyroclast dispersal distance, although calculating
717 these conditions is beyond the scope of this work.

718 Rutherford et al. (2017) devised a model for the ascent of high-Ti/orange picritic magma,
719 based on gas solubility experiments. High-temperature and -pressure experiments were used to
720 simulate magma ascent, in order to determine the type and abundance of volatile species that
721 would exsolve during the ascent of an analogue orange picrite. Matching depth in the conduit
722 with the corresponding temperature and pressure, three stages of lunar magma ascent were
723 interpreted: (1) 550 km depth, the source region of the picrite partial melt zone, up to 50 km
724 depth (2) 50-0.5 km depth: C, O, H, and S compounds exsolve from the magma, and (3) < 500 m
725 depth: volatile phases continue to exsolve within a closed system, with a gas volume fraction of
726 0.7 at a depth of ~130 m. While we only model to a depth of 10 km, it can be said that our results
727 partly match the gas volume fraction measured for stage 3 of the Rutherford et al. (2017) model;
728 indeed, we see an exit gas volume fraction of 0.7-0.8 for an intermediate-Ti, high volatile content
729 simulations (Figs. 3d and 4b). However, they conclude that fragmentation would take place at a
730 depth of 130 m, based on the reaching of a critical gas volume fraction (0.7) [Sparks et al.,
731 1978], or at a depth of 300-600 m, based on the pressure required to explain the carbon content
732 of the samples. Differences with the Rutherford et al. (2017) model likely stem from the different
733 initial volatile contents utilised (800-900 ppm H_2O and 1280 ppm CO) and from the different
734 fragmentation models incorporated. Our results suggest, based on the pressure and choked flow
735 conditions and the Deborah number, that fragmentation would occur once the magma exits the
736 vent, which is in agreement with the conclusions made by Rutherford and Papale (2009).

737 The distinction of lava fountaining as a separate eruption style from effusive and
738 explosive activity in terrestrial basaltic eruptions has recently been made by La Spina et al.
739 (2021). They show that for a lava fountaining eruption style, fragmentation does not occur within
740 the conduit, but above the vent. Our results are consistent with previous models that attribute the
741 lunar pyroclastic glass beads to lava fountaining [Carter et al., 2009; Coombs and Hawke, 1992;
742 Elkins-Tanton et al., 2003a], but also match the recent work that quantitatively defines lava
743 fountaining behaviour on Earth [La Spina et al., 2021]. Understanding the volume fractions of
744 gas present during ascent and eruption, as well as the point at which fragmentation occurs, is
745 important for understanding the emplacement of lunar pyroclastic deposits, in particular the size
746 distribution of pyroclasts and the extent of different deposits.

747 4.3 Comparison with volcanism on other planetary bodies

748 Many questions still exist regarding the volatile budget and style of volcanic activity
749 across the silicate bodies in our solar system [Horowitz et al., 2017; McCubbin et al., 2015;
750 Tartèse et al., 2013]. The surfaces of our Moon, Mercury, and Mars have been well-imaged by
751 various satellites, allowing us to make measurements of various volcanic features on these
752 bodies, such as lava flows and pyroclastic deposits. From this, some inferences have been made
753 on the volatile content of the different magmas that drove volcanic activity, which have been
754 paired with geochemical information to understand the volatile species that may have been

755 present. We briefly detail some of the progress that has been made in understanding the volatiles
756 that may have driven volcanism on Mercury and Mars, to put our work into context.

757   4.3.1 Mercury

758   Over fifty deposits mapped on Mercury's surface are thought to have been produced by
759 explosive volcanic activity [Goudge et al., 2014]. Mercurian pyroclastic deposits generally have
760 a greater areal extent than lunar pyroclastic deposits, which has led to the inference that
761 Mercury's pyroclastic eruptions involved greater amounts of volatiles than lunar pyroclastic
762 eruptions [Kerber et al., 2011]. Based on the age-relationships between pyroclastic deposits and
763 impact craters, Thomas et al. (2014) suggested that long-lived explosive volcanism occurred on
764 Mercury, spanning from ~3.9 to 1.0 Ga. Not only does this provide information on the thermal
765 history of Mercury, it also indicates that Mercury had a relatively substantial mantle volatile
766 inventory. Based on the highly reducing conditions likely present, it is unlikely that H_2O is
767 abundant in Mercury's mantle [Hirschmann et al., 2012]. Several volatiles have been proposed as
768 the main drivers of Mercury's explosive volcanic activity: S_2Cl, Cl, Cl_2, and COS [Kerber et al.,
769 2011], as well as H_2 and H_2S [Greenwood et al., 2018]. These studies verified results from a
770 chemical equilibrium model by Zolotov (2010), which suggested that N_2, CO, S_2, CS_2, S_2Cl, Cl,
771 Cl_2, and COS could make up a significant portion of Mercury's volcanic gases.

772   To give a sense of scale between our results and pyroclastic deposits on Mercury, we give
773 a brief comparison with a study by Kerber et al. (2009). Based on the morphology of a large
774 volcanic deposit in the Caloris impact basin, Kerber et al. (2009) calculated the minimum vent
775 speed and volatile content required to eject a pyroclast 24 km (the radius of the Caloris basin
776 pyroclastic deposit) from the vent. They calculated that a minimum exit velocity of 300 m s^{-1} and
777 volatile abundances of 3600 ppm (H_2O) and 5500 ppm (CO), which they calculated to be the
778 equivalent of 1600 ppm of H_2O and 2400 ppm of CO in lunar conditions. This suggests that the
779 volatile contents we modelled, which are based on measured and modelled volatile abundances
780 in lunar samples, would not propel pyroclasts to distances as far as the 24 km measured for the
781 Caloris basin pyroclastic deposit.

782   4.3.2 Mars

783   The majority of volcanic deposits on Mars that have been studied have been produced by
784 effusive volcanic activity [Glaze and Baloga, 2006; Hulme, 1976; Wilson et al., 2009]. Although
785 there are a growing number of studies looking at more cone-like deposits, produced by explosive
786 activity [Brož and Hauber, 2011; Lanz et al., 2010], there are still many connections to be made
787 between studies of volatiles in Mars' mantle, (such as Filiberto and Treiman (2009); Filiberto et
788 al. (2016)), and understanding the key volatile elements that drove explosive volcanic activity on
789 Mars.

790   Compared with Mercury, a much greater wealth of information on the volatile content
791 and oxygen fugacity of the Martian interior exists due to studies of Martian meteorites. The main
792 volatiles that have been studied include H_2O, C-species, S-species, F, and Cl. For H_2O, there has
793 been some debate over whether Martian meteorites are anhydrous [Leshin et al., 1996] or
794 whether they represent material that has completely degassed during eruption or emplacement
795 [McSween et al., 2001; Nekvasil et al., 2007]. A generally accepted value of 73-290 ppm H_2O in
796 the Martian mantle has been estimated from apatites found in shergottites [McCubbin et al.,
797 2012], which is on the same order of magnitude as current lunar estimates [Boyce et al., 2010;

798   Tartèse et al., 2013; Wang et al., 2012]. Based on geochemical and experimental constraints, it
799   has also been suggested that Cl and F were more abundant than H_2O in Martian magmas and
800   therefore may have had a greater influence on driving magma ascent and eruption [Filiberto et
801   al., 2016; Filiberto and Treiman, 2009].

802

803   4.4 Future model applications and developments

804   The links between volcanic deposit morphology and eruption conditions have been well
805   explored for a range of planetary bodies and features [Garry et al., 2007; Lena et al., 2008;
806   Moore et al., 1978; Wilson et al., 2009]. For the results presented here, we suggest that the
807   calculated mass flow rates (Table S4 in Supporting Information) could be paired with
808   measurements of the volumes of pyroclastic deposits [such as Trang et al., 2017] to provide
809   some estimates on the duration of eruptions on the Moon, which is poorly understood. Such
810   knowledge could provide useful insight into the repose time between periods of volatile release
811   on the lunar surface, helping to understand whether transient atmosphere(s) existed on the Moon
812   during periods of regular or pronounced volcanic activity [Head et al., 2020; Needham and
813   Kring, 2017]. The results of our sensitivity analysis showed that conduit radius had a very strong
814   control on the calculated mass eruption rate. Therefore, in order to produce these robust
815   estimates for eruption duration, the range of values used for the conduit radius would need to be
816   constrained with better certainty. As present, it has not been possible to resolve individual
817   magmatic conduits from lunar gravimetric data [Andrews-Hanna et al., 2013]; as more data
818   becomes available, this avenue could be explored more effectively.

819   There are several different aspects of lunar volcanism that could be investigated using the
820   magma ascent model used here. First of all, the ascent of high-Ti basalts could be investigated in
821   more detail. Although it is assumed that partial melts within the lunar crust would always
822   buoyantly ascend due to a sufficient density difference, Delano (1990) proposed that high-Ti
823   basalts would be an exception to this rule, calculating that high-Ti basalts would exceed a
824   "compositional limit of eruptability". Delano (1990) calculated that a TiO_2 content of roughly
825   16.4% would result in such a high density that any dykes would stall or even descend within the
826   mantle or crust. This value for TiO_2 content is difficult to verify: if samples of this magma are
827   not reaching the surface due to stalling, then there is an inherent bias in samples of picritic glass
828   beads, samples which we must base our modelled compositions on [Shearer et al., 1990]. While
829   we used the same density for all compositions of magma within the equations of state of the
830   model, the magma ascent model used here would be a fitting method for investigating the initial
831   conditions that would produce a theoretical limit, beyond which a magma would not ascend and
832   erupt.

833   Secondly, data from future missions could be used to infer the magma ascent model to
834   understand specific volcanic sites on the Moon, for example, samples collected by Chang'e 5
835   from northern Oceanus Procellarum. Compositional data could provide information for the initial
836   conditions of the magma ascent model, which could be used to simulate magma ascent in the
837   area. This could be particularly useful since the basalts near Chang'e 5's landing site are thought
838   to be some of the youngest mare basalts, with some areas of high-Ti basalt present [Qian et al.,
839   2021].

840

841 **5 Conclusions**

842   We have investigated the effect of different magmatic H- and C-species and volatile
843 contents on magma ascent dynamics, for the ascent of picritic magma within the lunar crust. We
844 have applied a 1-dimensional, multiphase numerical model, previously used for terrestrial cases
845 [de' Michieli Vitturi et al., 2011; La Spina et al., 2015, 2016, 2017, 2019, 2021] to a lunar
846 scenario. We also performed a sensitivity analysis to investigate the relationship between various
847 initial conditions and model outputs.

848   Using measured and modelled H_2, H_2O, and CO abundances in the numerical magma
849 ascent model and sensitivity analysis, we have shown that CO has a stronger control on the
850 magma ascent dynamics than H_2O, for model simulations investigating H_2O and CO. We can see
851 from gas exsolution profiles and Sobol indices that the range of H_2O abundances presented in
852 previous studies [Saal et al., 2008] do not have a large effect on magma ascent dynamics
853 compared with other initial conditions, namely CO abundance, temperature, pressure, and
854 conduit radius. Initial CO content had the strongest control on exit velocity and exit pressure,
855 which, in turn, strongly influence the formation of plumes, ejection of ballistics in the
856 surrounding area, and, ultimately, the deposits that we can observe on the surface of the Moon. It
857 is likely that initial CO content has a significant control on eruption style and eventual
858 pyroclastic deposit morphology, making it a key volatile for driving lunar volcanic eruptions.
859 This finding is in agreement with a number of studies [Rutherford et al., 2017; Rutherford and
860 Papale, 2009; Sato, 1979; Wilson and Head, 2017]. We conclude that understanding the
861 abundance and origin of CO is of great importance for understanding lunar magma ascent,
862 subsequent eruption processes, and deposit morphology.

863   For model simulations investigating H_2 and CO, we have shown that H_2 has a similar or
864 slightly greater control on magma ascent dynamics than CO. While some authors have suggested
865 that H_2 would be the dominant H-species driving lunar magma ascent and eruption [Renggli et
866 al. 2017], other studies have shown that H_2O would be the more abundant H-species present for
867 the conditions simulated in our magma ascent model [Hirschmann et al., 2012]. Overall, the
868 results from this study highlight the importance of factors such as oxygen fugacity, H content,
869 and pressure in understanding how H partitions between H_2O and H_2 in magmas, and, therefore,
870 how different volatile elements control magma ascent and eruption. In any case, for the ranges of
871 volatile abundances considered here, either H_2 or H_2O produce similar values (i.e. results for H_2
872 only 5-10% higher than for H_2O) for mass eruption rate, exit velocity, exit pressure, and exit gas
873 volume fraction, with, suggesting that the differences in plume dispersal or ballistic ejection
874 would not be significant.

875   Our results also showed that magma composition does not have a significant effect on the
876 overall magma ascent dynamics. The different compositions adopted affect the magma viscosity,
877 with an order of magnitude difference between the green/very low-Ti picrite (viscosity of ~1 Pa
878 s) to the black/high-Ti picrite (viscosity of ~10 Pa s). However, this variation in viscosity is not
879 enough to produce a significant variation in the magma ascent dynamics across the different
880 magmas, and thus differences in magma composition are unlikely to produce significant
881 differences in eruption style.

882   The methods used in this study could provide a wealth of information on many different
883 aspects of lunar volcanism, such as understanding lunar eruption processes in a quantitative way,
884 the role of different S-species in driving lunar eruptions, or the feasibility of the ascent of high-Ti

885 magmas. The application of increasingly sophisticated numerical models of magma ascent to
886 investigate planetary volcanism will only increase over time as more data (such as the interior
887 compositions, magmatic compositions, and volatile contents across different planetary bodies)
888 becomes available to the scientific community.

889

904

905

906

907

908

References

910 Adams, B. M., Bohnhoff, W. J., Dalbey, K. R., Ebeida, M. S., Eddy, J. P., Eldred, M. S.,
911 Geraci, G., Hooper, R. W., et al. (2014). *Dakota, a multilevel parallel object-oriented framework*
912 *for design optimization, parameter estimation, uncertainty quantification, and sensitivity*
913 *analysis.* (Version 6.11 User's Manual. Sandia Technical Report SAND2014-4633).
914 Albuquerque, New Mexico: Sandia National Laboratories.

915

916 Anand, M., Tartèse, R., & Barnes, J. J. (2014). Understanding the origin and evolution of water
917 in the Moon through lunar sample studies. *Philosophical Transactions of the Royal Society A*,
918 *372*, 20130254. https://doi.org/10.1098/rsta.2013.0254

919

920 Anderson, E. M. (1951). *The dynamics of faulting and dyke formation with applications to*
921 *Britain.* Edinburgh: Oliver and Boyd.

922

923 Andrews-Hanna, J.C., Asmar, S. W., Head, J. W., Kiefer, W. S., Konopliv, A. S., Lemoine, F.
924 G., Matsuyama, I., Mazarico, E., et al. (2013). Ancient Igneous Intrusions and Early Expansion

of the Moon Revealed by GRAIL Gravity Gradiometry. *Science, 93*, 675–678. https://doi.org/10.1126/science.1231753

Aravena., Á., de' Michieli Vitturi, M., Cioni, R., & Neri, A. (2017). Stability of volcanic conduits during explosive eruptions. *Journal of Volcanology and Geothermal Research, 339*, 52-62. https://doi.org/10.1016/j.jvolgeores.2017.05.003

Aravena, Á., de' Michieli Vitturi, M., Cioni, R., & Neri, A. (2018). Physical constraints for effective magma-water interaction along volcanic conduits during silicic explosive eruptions. *Geology*, *46* (10), 867-870. https://doi.org/10.1130/G45065.1

Arzilli, F., La Spina, G., Burton, M. R., Polacci M., Gall, N. L., Hartley, M. E., Genova, D. D., Cai, B., et al. (2019). Magma fragmentation in highly explosive basaltic eruptions induced by rapid crystallization. *Nature Geoscience, 10*, 1023-1028. https://doi.org/10.1038/s41561-019-0468-6

Baker, D. R., & Moretti, R. (2011). Modeling the Solubility of Sulfur in Magmas: A 50-Year Old Geochemical Challenge. *Reviews in Mineralogy and Geochemistry, 73*(1), 167–213. https://doi.org/10.2138/rmg.2011.73.7

Basaltic Volcanism Study Project (1981). *Basaltic Volcanism on the Terrestrial Planets*. New York: Pergamon Press Inc..

Binder, A. B. (1976). On the compositions and characteristics of the mare basalt magmas and their source regions. *The Moon, 16* (1), 115–150.

Blundy, J., Cashman, K., & Humphreys, M. (2006). Magma heating by decompression-driven crystallization beneath andesite volcanoes. *Nature, 443*, 76-80. https://doi.org/10.1038/nature05100

Boyce, J. W., Liu, Y., Rossman, G. R., Guan, Y., Eiler, J. M., Stolper, E. M., & Taylor, L. A. (2010). Lunar apatite with terrestrial volatile abundances. *Nature, 466* (7305), 466–469. https://doi.org/10.1038/nature09274

Braden, S. E., Stopar, J. D., Robinson, M. S., Lawrence, S. J., Van Der Bogert, C. H., & Hiesinger, H. (2014). Evidence for basaltic volcanism on the Moon within the past 100 million years. *Nature Geoscience, 7* (11), 787–791. https://doi.org/10.1038/ngeo2252

Brown, G. O. (2002). *The history of the Darcy-Weisbach equation for pipe flow resistance.* Paper presented at Environmental and Water Resources History Sessions at ASCE Civil Engineering Conference and Exposition, Washington, D.C., United States. https://doi.org/10.1061/40650(2003)4

Brown, S. M., & Grove, T. L. (2015). Origin of the Apollo 14, 15, and 17 yellow ultramafic glasses by mixing of deep cumulate remelts. *Geochimica et Cosmochimica Acta, 171*, 201-215. https://doi.org/10.1016/j.gca.2015.09.001

Brož, P., & Hauber, E. (2011). A unique volcanic field in Tharsis, Mars: Pyroclastic cones as evidencefor explosive eruptions. *Icarus, 218*, 88-99. https://doi.org/10.1016/j.icarus.2011.11.030

Caricchi, L., Burlini, L., Ulmer, P., Gerya, T., Vassalli, M., & Papale, P. (2007). Non-Newtonian rheology of crystal-bearing magmas and implications for magma ascent dynamics. *Earth and Planetary Science Letters, 264*, 402-419. https://doi.org/10.1016/j.epsl.2007.09.032

Carr, B. B., Clarke, A. B., & de' Michieli Vitturi, M. (2018). Earthquake induced variations in extrusion rate: A numerical modeling approach to the 2006 eruption of Merapi Volcano (Indonesia). *Earth and Planetary Science Letters, 482*, 377–387. https://doi.org/10.1016/j.epsl.2017.11.019

Carter, L. M., Campbell, B. A., Hawke, B. R., Campbell, D. B., & Nolan, M. C. (2009). Radar remote sensing of pyroclastic deposits in the southern Mare Serenitatis and Mare Vaporum regions of the Moon. *Journal of Geophysical Research: Planets, 114*, 1–12. https://doi.org/10.1029/2009JE003406

Colebrook, F. (1939). Turbulent flow in pipes with particular reference to the transition region between the smooth and rough pipe laws. *Journal of the Institution of Civil Engineers, 4*, 14–25. https://doi.org/10.1680/ijoti.1939.13150

Coombs, C., & Hawke, B. R. (1992). Pyroclastic Deposits on the Western Limb of the Moon. In *Proceedings of the Lunar and Planetary Science Conference, 22*, 303-312. Houston, Texas: Lunar and Planetary Institute.

Costa, A. (2005). Viscosity of high crystal content melts: Dependence on solid fraction. *Geophysical Research Letters*, *32*, L22308. https://doi.org/doi:10.1029/2005GL024303

Costa, A., Caricchi, L., & Bagdassarov, N. (2009). A model for the rheology of particle-bearing suspensions and partially molten rocks. *Geochemistry, Geophysics, Geosystems, 10*, Q03010. https://doi.org/10.1029/2008GC002138

Costa, A. L., Melnik, O., & Vedeneeva, E. (2007). Thermal effects during magma ascent in conduits. *Journal of Geophysical Research: Solid Earth, 112* (B12205). https://doi.org/doi:10.1029/2007JB004985

De' Michieli Vitturi, M., Clarke, A. B., Neri, A., & Voight, B. (2008). Effects of conduit geometry on magma ascent dynamics in dome-forming eruptions. *Earth and Planetary Science Letters, 272* (3-4), 567-578. https://doi.org/10.1016/j.epsl.2008.05.025

De' Michieli Vitturi, M., Clarke, A. B., Neri, A., & Voight, B. (2010). Transient effects of magma ascent dynamics along a geometrically variable dome-feeding conduit. *Earth and Planetary Science Letters, 295*, 541-553. https://doi.org/10.1016/j.epsl.2010.04.029

De' Michieli Vitturi, M., Clarke, A. B., Neri, A., & Voight, B. (2011). *Assessing the influence of disequilibrium crystallization and degassing during magma ascent in effusive and explosive eruptions (#V23H-05).* Paper presented at American Geophysical Union Fall Meeting, San Francisco, California, United States.

Degruyter, W., Bachmann, O., Burgisser, A., & Manga, M. (2012). The effects of outgassing on the transition between effusive and explosive silicic eruptions. *Earth and Planetary Science Letters, 349-350*, 161-170. https://doi.org/10.1016/j.epsl.2012.06.056

Delano, J. W. (1980). Chemistry and liquidus phase relations of Apollo 15 red glass: Implications for the deep lunar interior. In *Proceedings of the Lunar and Planetary Science Conference, 11,* 251-288. Houston, Texas: Lunar and Planetary Institute.

Delano, J.W. (1986). Pristine lunar glasses: Criteria, data, and implications. *Journal of Geophysical Research: Solid Earth*, *91*(B4), 201-213. https://doi.org/10.1029/JB091iB04p0D201

Delano, J. W. (1990). Buoyancy-driven Melt Segregation in the Earth's Moon, I. Numerical Results. In *Proceedings of the Lunar and Planetary Science Conference, 20*, 3-12. Houston, Texas: Lunar and Planetary Institute.

Delano, J. W., & Lindsley, D. H. (1983). Mare Glasses From Apollo 17: Constraints on the Moon's Bulk Composition. In *Proceedings of the Lunar and Planetary Science Conference, 14*, B3-B16. Houston, Texas: Lunar and Planetary Institute.

Delano, J. W., & Livi, K. (1981). Lunar volcanic glasses and their constraints on mare petrogenesis. *Geochimica et Cosmochimica Acta, 45*, 2137-2149. https://doi.org/10.1016/0016-7037(81)90066-1

Dingwell, D. B., & Webb, S. L. (1989). Structural relaxation in silicate melts and non-Newtonian melt rheology in geologic processes. *Physics and Chemistry of Minerals, 16*, 508–516. https://doi.org/10.1007/BF00197020

Elkins-Tanton, L. T., Chatterjee, N., & Grove, T. L. (2003a). Magmatic processes that produced lunar fire fountains. *Geophysical Research Letters, 30* (10), D505-D508. https://doi.org/10.1029/2003GL017082

Elkins-Tanton, L. T., Chatterjee, N., & Grove, T. L. (2003b). Experimental and petrological constraints on lunar differentiation from the Apollo 15 green picritic glasses. *Meteoritics & Planetary Science, 38*(4), 515-27. https://doi.org/10.1111/j.1945-5100.2003.tb00024.x

Fang, X., Xu, Y., & Zhou, Z. (2011). New correlations of single-phase friction factor for turbulent pipe flow and evaluation of existing single-phase friction factor correlations. *Nuclear Engineering and Design, 241*, 897–902. https://doi.org/10.1016/j.nucengdes.2010.12.019

Fogel, R. A., & Rutherford, M. J. (1995). Magmatic volatiles in primitive lunar glasses: I. FTIR and EPMA analyses of Apollo 15 green and yellow glasses and revision of the volatile-assisted

fire-fountain theory. *Geochimica et Cosmochimica Acta, 59*, 201–215.
https://doi.org/10.1016/0016-7037(94)00377-X

Filiberto, J., Gross, J., & McCubbin, F. M. (2016). Constraints on the water, chlorine, and
fluorine content of the Martian mantle. *Meteoritics and Planetary Science, 51* (11), 2023-2035.
https://doi.org/10.1111/maps.12624

Filiberto, J., & Treiman, A. H. (2009). Martian magmas contained abundant chlorine, but little
water. *Geology, 37* (12), 1087-1090. https://doi.org/10.1130/G30488A

Gaddis, L. R., Hawke, B. R., Robinson, M. S., & Coombs, C. (2000). Compositional analyses of
small lunar pyroclastic deposits using Clementine multispectral data. *Journal of Geophysical
Research: Planets, 105*, 4245–4262. https://doi.org/10.1029/1999JE001070

Gaddis, L. R., Pieters, C. M., & Hawke, B. R. (1985). Remote Sensing of Lunar Pyroclastic
Mantling Deposits. *Icarus, 61*, 461–489. https://doi.org/10.1016/0019-1035(85)90136-8

Gaddis, L. R., Staid, M. I., Tyburczy, J. A., Hawke, B. R., & Petro, N. E. (2003). Compositional
analyses of lunar pyroclastic deposits. *Icarus*, *161*(2), 262-280. https://doi.org/10.1016/S0019-
1035(02)00036-2

Garry, W. B., Zimbelman, J. R., & Gregg, T. K. P. (2007). Morphology and emplacement of a
long-channelled lava flow near Ascraeus Mons Volcano, Mars. *Journal of Geophysical
Research, 112* (E08007), 1-21. https://doi.org/10.1029/2006JE002803

Gerlach, T. M., McGee, K. A., Elias, T., Sutton, A. J., & Doukas, M. P. (2002). Carbon dioxide
emission rate of Kilauea volcano: Implications for primary magma and the summit reservoir:
Journal of Geophysical Research, 107 (B9), 2189. https://doi.org/10.1029/2001JB00040

Ghiorso, M. S., & Gualda, G. A. R. (2015). An H_2O–CO_2 mixed fluid saturation model
compatible with rhyolite-MELTS. *Contributions to Mineralogy and Petrology,* 169 (53).
https://doi.org/10.1007/s00410-015-1141-8

Giordano, D., & Dingwell, D. B. (2003). Viscosity of hydrous Etna basalt: implications for
Plinian-style basaltic eruptions. *Bulletin of Volcanology, 65*, 8-14.
https://doi.org/10.1007/s00445-002-0233-2

Giordano, D., Russell, J. K., & Dingwell, D. B. (2008). Viscosity of magmatic liquids: a model.
Earth and Planetary Science Letters, 271, 123-134. https://doi.org/10.1016/j.epsl.2008.03.038

Glaze, L. S., & Baloga, S. M. (2006). Rheologic inferences from the levees of lava flows on
Mars. *Journal of Geophysical Research,* 111 (E09006), 1-10.
https://doi.org/10.1029/2005JE002585

Goudge, T. A., Head, J. W., Kerber, L., Blewett, D. T., Denevi, B. W., Domingue, D. L., Gillis-
Davis, J. J., Gwinner, K., et al. (2014). Global inventory and characterization of pyroclastic

1108 deposits on Mercury: new insights into pyro-clastic activity from MESSENGER orbital data.
1109 *Journal of Geophysical Research, 119*, 635-658. https://doi.org/10.1002/2013JE004480

1111 Greenwood, J. P., Karato, S., Vander Kaaden, K. E., Pahlevan, K., & Usui, T. (2018). Water and
1112 Volatile Inventories of Mercury, Venus, the Moon, and Mars. *Space Science Reviews, 214*(5).
1113 https://doi.org/10.1007/s11214-018-0526-1

1115 Grove, T. L., & Krawczynski, M. J. (2009). Lunar mare volcanism: where did the magmas come
1116 from? *Elements, 5* (1), 29-34. https://doi.org/10.2113/gselements.5.1.29

1118 Gualda, G. A. R., Ghiorso, M. S., Lemons, R. V., & Carley, T. L. (2012). Rhyolite-MELTS: a
1119 Modified Calibration of MELTS Optimized for Silica-rich, Fluid-bearing Magmatic Systems.
1120 *Journal of Petrology, 53*, 875-890. https://doi.org/10.1093/petrology/egr080

1122 Gustafson, J. O., Bell, J. F., Gaddis, L. R., Hawke, B. R., & Giguere, T. A. (2012).
1123 Characterization of previously unidentified lunar pyroclastic deposits using Lunar
1124 Reconnaissance Orbiter Camera data. *Journal of Geophysical Research, 117*, 1–21.
1125 https://doi.org/10.1029/2011JE003893

1127 Hartmann, W. K. (2014). The giant impact hypothesis: past, present (and future?). *Philosophical
1128 Transactions of the Royal Society A, 372*, 20130249. https://doi.org/10.1098/rsta.2013.0249

1130 Hartmann, W.K., & Davis, D.R. (1974). Satellite-sized planetesimals and lunar origin. *Icarus, 24*
1131 (4), 504-515. https://doi.org/10.1016/0019-1035(75)90070-6

1133 Hauri, E. H., Weinreich, T., Saal, A. E., Rutherford, M. C., & Van Orman, J. A. (2011). High
1134 Pre-Eruptive Water Contents Preserved in Lunar Melt Inclusions. *Science, 333*, 213–216.
1135 https://doi.org/10.1126/science.1204626

1137 Hawke, B. R., Coombs, C., Gaddis, L. R., Lucey, P. G., & Owensby, P. D. (1989). Remote
1138 Sensing and Geologic Studies of Localized Dark Mantle Deposits on the Moon. In *Proceedings
1139 of the Lunar Science Conference, 19*, 255–268. Houston, Texas: Lunar and Planetary Institute.

1141 Head, J. W., & Wilson, L. (1979). Alphonsus-type dark-halo craters: Morphology, morphometry
1142 and eruption conditions. In *Proceedings of the Lunar and Planetary Science Conference, 10,*
1143 2861-2897. Houston, Texas: Lunar and Planetary Institute.

1145 Head, J. W., & Wilson, L. (2017). Generation, ascent and eruption of magma on the Moon: New
1146 insights into source depths, magma supply, intrusions and effusive/explosive eruptions (Part 2:
1147 Predicted emplacement processes and observations). *Icarus, 283*, 176-223.
1148 https://doi.org/10.1016/j.icarus.2015.12.039

1150 Head, J. W., Wilson, L., Deutsch, A. N., Rutherford, M. J., & Saal, A. J. (2020). Volcanically
1151 Induced Transient Atmospheres on the Moon: Assessment of Duration, Significance, and
1152 Contributions to Polar Volatile Traps. *Geophysical Research Letters, 47* (18), e2020GL089509.
1153 https://doi.org/10.1029/2020GL089509

Heiken, G. H., McKay, D. S., & Brown, R. W. (1974). Lunar deposits of possible pyroclastic origin. *Geochimica et Cosmochimica Acta, 38*, 1703-1704. https://doi.org/10.1016/0016-7037(74)90187-2

Hekinian, R., Pineau, F., Shilobreeva, S., Bideau, D., Gracia, E., & Javoy, M. (2000). Deep sea explosive activity on the Mid-Atlantic Ridge near 34°50′ N: Magma composition, vesicularity, and volatile content. *Journal of Volcanology and Geothermal Research, 98*, 4. https://doi.org/10.1016/S0377-0273(99)00190-0

Hess, P. C. (2000). On the source region for mare picritic glasses. *Journal of Geophysical Research, 105* (E2), 4347-4360. https://doi.org/10.1029/1999JE001067

Hiesinger, H., Head, J. W., Wolf, U., Jaumann, R., & Neukum, G. (2011). Ages and stratigraphy of lunar mare basalts: A synthesis. *GSA Special Papers, 477*, 1–51. https://doi.org/10.1029/2009JE003380

Hirschmann, M. M., Withers, A. C., Ardia, P., & Foley, N. T. (2012). Solubility of molecular hydrogen in silicate melts and consequences for volatile evolution of terrestrial planets. *Earth and Planetary Science Letters, 345–348*, 38–48. https://doi.org/10.1016/j.epsl.2012.06.031

Holloway, J.R., & Blank, J.G. (1994). Application of experimental results to C–O–H species in natural melts. In Volatiles In Magmas. *Reviews in Mineralogy*, 30, 187–230.

Horowitz, H. M., Jacob, D. J., Zhang, Y., Dibble, T. S., Slemr, F., Amos, H. M., Schmidt, J. A., Corbitt, E. S., et al. (2017). A new mechanism for atmospheric mercury redox chemistry: implications for the global mercury budget. *Atmospheric Chemistry and Physics*, 17, 6353-6371. https://doi.org/10.5194/acp-17-6353-2017

Hughes, S. S., Delano, J. W., & Schmitt, R. A. (1988). Apollo 15 yellow-brown volcanic glass: Chemistry and petrogenetic relations to green volcanic glass and olivine-normative mare basalts. *Geochimica et Cosmochimica Acta, 52*, 2379-2391. https://doi.org/10.1016/0016-7037(88)90295-5

Hulme, G. (1976). The determination of the rheological properties and effusion rate of an Olympus Mons lava. *Icarus, 27* (2), 207-213. https://doi.org/10.1016/0019-1035(76)90004-X

Iman, R. L., & Conover, W. J. (1980). Small sample sensitivity analysis techniques for computer models with an application to risk assessment. *Communications in Statistics – Theory and Methods, 9* (17), 1-95. https://doi.org/10.1080/03610928008827996

Jolliff, B. L. Wieczorek, M. A., Shearer, C. K., & Neal, C. R. (2006). *New Views of the Moon*. Berlin: De Gruyter.

Jones, T. J., Reynolds, C. D., & Boothroyd, S. C. (2019). Fluid dynamic induced break-up during volcanic eruptions. *Nature Communications, 10*, 3828. https://doi.org/10.1038/s41467-019-11750-4

Kavanagh, J. L., & Sparks, R. S. J. (2011). Insights of dyke emplacement mechanics from detailed 3D dyke thickness datasets. *Journal of the Geological Society, 168*, 965-978. https://doi.org/10.1144/0016-76492010-137

Kerber, L., Head, J. W., Solomon, S. C., Murchie, S. L., Blewett, D. T., & Wilson, L. (2009). Explosive volcanic eruptions on Mercury: eruption conditions, magma volatile content, and implications for mantle volatile abundances. *Earth and Planetary Science Letters, 285*, 263e271. https://doi.org/10.1016/j.epsl.2009.04.037

Kerber, L., Head, J.W., Blewett, D.T., Solomon, S.C., Wilson, L., Murchie, S.L., Robinson, M.S., Denevi, B.W., et al. (2011). The global distribution of pyroclastic deposits on Mercury: the view from MESSENGER flybys 1–3. *Planetary and Space Science, 59*, 1895–1909. https://doi.org/10.1016/j.pss.2011.03.020

Kerber, L., Head, J. W., Solomon, S., Murchie, S., Blewett, D., & Wilson, L. (2009). Explosive volcanic eruptions on Mercury: eruption conditions, magma volatile content, and implications for interior volatile abundances. *Earth and Planetary Science Letters*, *285*(3-4), 263-271. https://doi.org/10.1016/j.epsl.2009.04.037

Klausen, M. B. (2006). Similar dyke thickness variation across three volcanic rifts in the North Atlantic region: Implications for intrusion mechanisms. *Lithos, 92* (1-2), 137-152. https://doi.org/10.1016/j.lithos.2006.03.030

Lanz, J. K., Wagner, R., Wolf, U., Kröchert, J., & Neukum, G. (2010). Rift zone volcanism and associated cinder cone field in Utopia Planitia, Mars. *Journal of Geophysical Research: Planets, 115* (E12019), 1-21. https://doi.org/10.1029/2010JE003578

La Spina, G., Clarke, A. B., de' Michieli Vitturi, M., Burton, M. R., Allison, C. M., Roggensack, K., & Alfano, F. (2019). Conduit dynamics of highly explosive basaltic eruptions: The 1085 CE Sunset Crater sub-Plinian events. *Journal of Volcanology and Geothermal Research, 387*, 106658. https://doi.org/10.1016/j.jvolgeores.2019.08.001

La Spina, G., Arzilli, F., Llewellin, E. W., Burton, M. R., Clarke, A. B., de' Michieli Vitturi, M., Polacci, M., Hartley, et al. (2021). Explosivity of basaltic lava fountains is controlled by magma rheology, ascent rate and outgassing. *Earth and Planetary Science Letters, 553,* 1-11. https://doi.org/10.1016/j.epsl.2020.116658

La Spina, G., Burton, M. R., & de' Michieli Vitturi, M. (2015). Temperature evolution during magma ascent in basaltic effusive eruptions: A numerical application to Stromboli volcano. *Earth and Planetary Science Letters, 426*, 89-100. https://doi.org/10.1016/j.epsl.2015.06.015

La Spina, G., Burton, M. R., de' Michieli Vitturi, M., & Arzilli, F. (2016). Role of syn-eruptive plagioclase disequilibrium crystallization in basaltic magma ascent dynamics. *Nature Communications, 7*, 13402. https://doi.org/10.1038/ncomms13402

La Spina, G., & de' Michieli Vitturi, M. (2012). High-Resolution Finite Volume Central Schemes for a Compressible Two-Phase Model. *SIAM Journal on Scientific Computing, 34*, B861-B880. https://doi.org/10.1137/12087089X

La Spina, G., de' Michieli Vitturi, M., & Romenski, E. (2014). A compressible single-temperature conservative two-phase model with phase transitions. *International Journal for Numerical Methods in Fluids, 76*, 282-311. https://doi.org/10.1002/fld.3934

La Spina, G., Polacci, M., Burton, M. R., & de' Michieli Vitturi, M. (2017). Numerical investigation of permeability models for low viscosity magmas: Application to the 2007 Stromboli effusive eruption. *Earth and Planetary Science Letters, 473*, 279–290. https://doi.org/10.1016/j.epsl.2017.06.013

Le Bas, M. J. (2000). IUGS reclassification of the high-Mg and picritic volcanic rocks. *Journal of Petrology, 41* (10), 1467-1470. https://doi.org/10.1093/petrology/41.10.1467

Lena, R., Wöhler, C., Bregante, M. T., Lazzarotti, P., & Lammel, S. (2008). Lunar domes in Mare Undarum: Spectral and morphometric properties, eruption conditions, and mode of emplacement. *Planetary and Space Science, 56* (3-4), 553-569. https://doi.org/10.1016/j.pss.2007.11.010

Leshin, L. A., Epstein, S., & Stolper, E. M. (1996). Hydrogen isotope geochemistry of SNC meteorites. *Geochimica et Cosmochimica Acta, 60*, 2635–2650. https://doi.org/10.1016/0016-7037(96)00122-6

Lister, J.R., & Kerr, R. C. (1991). Fluid-Mechanical Models of Crack Propagation and Their Application to Magma Transport in Dykes. *Journal of Geophysical Research, 96* (B6), 10049-10077. https://doi.org/10.1029/91JB00600

Llewellin, E. W., Mader, H. M., & Wilson, S. D. R. (2002). The constitutive equation and flow dynamics of bubbly magmas. *Geophysical Research Letters, 29*, 2170. https://doi.org/10.1029/2002GL015697

Mader, H. M., Llewellin, E. W., & Mueller, S. P. (2013). The rheology of two-phase magmas: a review and analysis. *Journal of Volcanology and Geothermal Research, 257*, 135–158. https://doi.org/10.1016/j.jvolgeores.2013.02.014

McCubbin F. M., Hauri E. H., Elardo S. M., Vander Kaaden K. E., Wang J., & Shearer C. K. (2012). Hydrous melting of the Martian mantle produced both depleted and enriched shergottites. *Geology, 40*, 683–686. https://doi.org/10.1130/G33242.1

McCubbin F. M., Vander Kaaden K. E., Tartèse R., Klima R. L., Liu Y., Mortimer J., Barnes J. J., Shearer C. K., et al. (2015). Magmatic volatiles (H, C, N, F, S, Cl) in the lunar mantle, crust, and regolith: Abundances, distributions, processes, and reservoirs. *American Mineralogist, 100*, 1668–1707. https://doi.org/10.2138/am-2015-4934CCBYNCND

McKay, M. D., Beckman, R. J., & Conover, W. J. (1979). A Comparison of Three Methods for Selecting Values of Input Variables in the Analysis of Output from a Computer Code. *Technometrics, 42* (1), 55-61. https://doi.org/10.1080/00401706.1979.10489755

McSween, H. Y., Grove, T. L., Lentz, R. C., Dann, J. C., Holzheid, A. H., Riciputi, L. R., & Ryan, J. G. (2001). Geochemical evidence for magmatic water within Mars from pyroxenes in the Shergotty meteorite. *Nature, 409*, 487–490. https://doi.org/10.1038/35054011

Melnik, O., & Sparks, R. S. J. (2002). Dynamics of magma ascent and lava extrusion at Soufrière Hills Volcano, Montserrat. *Geological Society, London, Memoirs, 21*, 153-171. https://doi.org/10.1144/GSL.MEM.2002.021.01.07

Moore, H. J., Arthur, W., & Schaber, G. G. (1978). Yield strengths of flows on Earth, Mars, and Moon. In *Proceedings of the Lunar and Planetary Science Conference, 9,* 3351–3378. Houston, Texas: Lunar and Planetary Institute.

Moore, G., Vennemann, T., & Carmichael, I. S. E. (1995). Solubility of water in magmas to 2 kbar. *Geology, 23 (12)*, 1099-1102. https://doi.org/10.1130/0091-7613(1995)023%3C1099:SOWIMT%3E2.3.CO;2

Moore, G., Vennemann, T., & Carmichael, I. S. E. (1998). An empirical model for the solubility of H_2O in magmas to 3 kilobars. *American Mineralogist, 83* (1-2), 36-42. https://doi.org/10.2138/am-1998-1-203

Morgan, C., Wilson, L., & Head, J. W. (2021). Formation and dispersal of pyroclasts on the Moon: Indicators of lunar magma volatile contents. *Journal of Volcanology and Geothermal Research, 413*, 107217. https://doi.org/10.1016/j.jvolgeores.2021.107217

Moune, S., Faure, F., Gauthier, P.-J., & Sims, K. W. W. (2007). Pele's hairs and tears: Natural probe of volcanic plume. *Journal of Volcanology and Geothermal Research, 164*, 244-253. https://doi.org/10.1016/j.jvolgeores.2007.05.007

Mysen, B. O., & Wheeler, K. (2000). Solubility behavior of water in haploandesitic melts at high pressure and high temperature. *American Mineralogist, 85 (9)*, 1128-1142. https://doi.org/10.2138/am-2000-8-903

Namiki, A. & Manga, M. (2008). Transition between fragmentation and permeable outgassing of low viscosity magmas. *Journal of Volcanology and Geothermal Research, 169*, 48–60. https://doi.org/10.1016/j.jvolgeores.2007.07.020

Neal, C. R., & Taylor, L. A. (1992). Petrogenesis of mare basalts: A record of lunar volcanism. *Geochimica et Cosmochimica Acta, 56* (6), 2177–2211. https://doi.org/10.1016/0016-7037(92)90184-K

Needham, D. H., & Kring, D. A. (2017). Lunar volcanism produced a transient atmosphere around the ancient Moon. *Earth and Planetary Science Letters, 478*, 175-178. https://doi.org/10.1016/j.epsl.2017.09.002

Nekvasil, H., Filiberto, J., McCubbin, F. M., & Lindsley, D. H. (2007). Alkalic parental magmas for the chassignites? *Meteoritics & Planetary Science, 42*, 979–992. https://doi.org/10.1111/j.1945-5100.2007.tb01145.x

Nicholis, M. G., & Rutherford, M. J. (2009) Graphite oxidation in the Apollo 17 orange glass magma: Implications for the generation of a lunar volcanic gas phase. *Geochimica et Cosmochimica Acta, 73*, 5905–5917. https://doi.org/10.1016/j.gca.2009.06.022

Papale, P. (1999). Strain-induced magma fragmentation in explosive eruptions. *Nature, 397*, 425–428. https://doi.org/10.1038/17109

Papale, P. (2001). Dynamics of magma flow in volcanic conduits with variable fragmentation efficiency and nonequilibrium pumice degassing. *Journal of Geophysical Research: Solid Earth, 106* (B6), 11043-11065. https://doi.org/10.1029/2000JB900428

Papale, P., & Dobran, F. (1994). Magma flow along the volcanic conduit during the Plinian and pyroclastic flow phases of the May 18, 1980, Mount St. Helens eruption. *Journal of Geophysical Research, 99* (B3), 4355-4373. https://doi.org/10.1029/93JB02972

Qian, Y., Xiao, L., Head, J. W., van der Bogert, C. H., Hiesinger, H., & Wilson, L. (2021). Young lunar mare basalts in the Chang'e-5 sample return region, northern Oceanus Procellarum. *Earth and Planetary Science Letters, 555*, 116702. https://doi.org/10.1016/j.epsl.2020.116702

Renggli, C. J., King, P. L., Henley, R. W., & Norman, M. D. (2017). Volcanic gas composition, metal dispersion and deposition during explosive volcanic eruptions on the Moon. *Geochimica et Cosmochimica Acta, 206*, 296-311. https://doi.org/10.1016/j.gca.2017.03.012

Rodio, M. G., & Abgrall, R. (2015). An innovative phase transition modeling for reproducing cavitation through a five-equation model and theoretical generalization to six and seven-equation models. *International Journal of Heat and Mass Transfer, 89*, 1386-1401. https://doi.org/10.1016/j.ijheatmasstransfer.2015.05.008

Romenski, E., Drikakis, D., & Toro, E. (2010). Conservative Models and Numerical Methods for Compressible Two-Phase Flow. *Journal of Scientific Computing, 42*, 68-95. https://doi.org/10.1007/s10915-009-9316-y

1377 Rutherford, M. J., Head, J. W., Saal, A. E., Hauri, E. H., & Wilson, L. (2017). Model for the
1378 origin, ascent, and eruption of lunar picritic magmas. *American Mineralogist, 102* (10), 2045–
1379 2053. https://doi.org/10.2138/am-2017-5994ccbyncnd
1380
1381 Rutherford, M. J., & Papale, P. (2009). Origin of basalt fire-fountain eruptions on Earth versus
1382 the Moon. *Geology, 37* (3), 219–222. https://doi.org/10.1130/G25402A.1
1383
1384 Saal, A. E., Hauri, E. H., Lo Cascio, M., Van Orman, J. A., Rutherford, M. C., & Cooper, R. F.
1385 (2008). Volatile content of lunar volcanic glasses and the presence of water in the Moon's
1386 interior. *Nature, 454*, 192-196. https://doi.org/10.1038/nature07047
1387
1388 Sato, M. (1979). The driving mechanism of lunar pyroclastic eruptions inferred from the oxygen
1389 fugacity behaviour of Apollo 17 orange glass. In *Proceedings of the Lunar and Planetary*
1390 *Science Conference, 10*, 311-325. Houston, Texas: Lunar and Planetary Institute.
1391
1392 Sharp, Z. D., McCubbin, F. M., & Shearer, C. M. (2011). *A Unifying Theory for Lunar Water*.
1393 Paper presented at American Geophysical Union Fall Meeting, San Francisco, California, United
1394 States.
1395
1396 Shearer, C. K., Hess, P. C., Wieczorek, M. A., Pritchard, M. E., Parmentier, E. M., Borg, L.E.,
1397 Longhi, J., Elkins-Tanton, L. E., et al. (2006). Thermal and Magmatic Evolution of the Moon.
1398 *Reviews in Mineralogy and Geochemistry, 60* (1), 365–518.
1399 https://doi.org/10.2138/rmg.2006.60.4
1400
1401 Shearer, C. K., & Papike, J. J. (1993). Basaltic magmatism on the Moon: A perspective from
1402 volcanic picritic glass beads. *Geochimica et Cosmochimica Acta, 57*, 4785-4812.
1403 https://doi.org/10.1016/0016-7037(93)90200-G
1404
1405 Shearer, C.K., & Papike, J.J. (2004). Oxygen Fugacity of Lunar Basalts and the Lunar Mantle.
1406 Range of fO_2 and the Effectiveness of Oxybarometers. In Workshop on Oxygen in the Terrestrial
1407 Planets, #3025. LPI Contribution No. 1203, Lunar and Planetary Institute, Houston.
1408
1409 Shearer, C. K., Papike, J. J., Simon, S. B., Shimizu, N., Yurimoto, Y., & Sueno, S. (1990). Ion
1410 microprobe studies of trace elements in Apollo 14 volcanic glass beads: Comparisons to Apollo
1411 14 mare basalts and petrogenesis of picritic magmas. *Geochimica et Cosmochimica Acta, 54*,
1412 851-867. https://doi.org/10.1016/0016-7037(90)90378-X
1413
1414 Sigurdsson, H. (2015). *The Encyclopedia of Volcanoes*. Amsterdam: Elsevier.
1415
1416 Spera, F. J. (1992). Lunar magma transport phenomena. *Geochimica et Cosmochimica Acta, 56*
1417 (6), 2253-2265. https://doi.org/10.1016/0016-7037(92)90187-N
1418
1419 Spudis, P. D. (2015). Volcanism on the Moon. In Sigurdsson, H. (Eds.), *The Encyclopedia of*
1420 *Volcanoes* (pp. 689-700). Amsterdam: Elsevier.
1421

Steele, A., McCubbin, F. M., Fries, M., Glamoclija, M., Kater, L., & Nekvasil, H. (2010) Graphite in an Apollo 17 impact melt breccia. *Science, 329*, 51. https://doi.org/10.1126/science.1190541

Tartèse, R., Anand, M., Barnes, J. J., Starkey, N. A., Franchi, I. A., & Sano, Y. (2013). The abundance, distribution, and isotopic composition of Hydrogen in the Moon as revealed by basaltic lunar samples: Implications for the volatile inventory of the Moon. *Geochimica et Cosmochimica Acta, 122*, 58–74. https://doi.org/10.1016/j.gca.2013.08.014

Taylor, G. J., Warren, P., Ryder, G., Delano, J., Pieters, C., & Lofgren, G. (1991). Lunar Rocks. In Heiken, G. H., Vaniman, D. T., and French, B. M. (Eds.), *Lunar Sourcebook* (pp. 183-284). Cambridge: Cambridge University Press.

Thomas, R. J., Rothery, D. A., Conway, S. J., & Anand, M. (2014), Long-lived explosive volcanism on Mercury. *Geophysical Research Letters, 41*, 6084–6092. https://doi.org/10.1002/2014GL061224

Thomas-Keprta, K. L., Clemett, S. J., Messenger, S., Ross, D. K., Le, L., Rahman, Z., McKay, D. S., Gibson Jr, E. K., et al. (2014). Organic matter on the Earth's Moon. *Geochimica et Cosmochimica Acta*, *134*, 1-15. https://doi.org/10.1016/j.gca.2014.02.047

Trang, D., Gillis-Davis, J. J., Lemelin, M., Cahill, J. T. S., Hawke, B. R., Giguere, T. A. (2017). The compositional and physical properties of localized lunar pyroclastic deposits. *Icarus, 283*, 232–253. https://doi.org/10.1016/j.icarus.2016.09.025

Wang, Y., Guan, Y., Hsu, W., & Eiler, J. M. (2012). *Water content, chlorine and hydrogen isotope compositions of lunar apatite.* Paper presented at 75th Annual Meteoritical Society Meeting, Cairns, Australia.

Webb, S. L., & Dingwell, D. B. (1990). The onset of non-Newtonian rheology of silicate melts. *Physics and Chemistry of Minerals, 17*, 125–132. https://doi.org/10.1007/BF00199663

Weisbach, J. L. (1845). Lehrbuch der Ingenieur- und Maschinen-Mechanik: ohne Anwendung des höhern Calculs für den Unterricht an technischen Lehranstalten sowie zum Gebrauche für Techniker : in zwei Theilen. Berlin: Vieweg.

Weitz, C. M., Head, J. W., & Pieters, C. M. (1998). Lunar regional dark mantle deposits: Geologic, multispectral, and modelling studies. *Journal of Geophysical Research: Planets*, *103* (E10), 22725-22759. https://doi.org/10.1029/98JE02027

Wetzel, D. T., Hauri, E. H., Saal, A. E., & Rutherford, M. J. (2015). Carbon content and degassing history of the lunar volcanic glasses. *Nature Geoscience, 8* (10), 755–758. https://doi.org/10.1038/ngeo2511

Wetzel, D. T., Rutherford, M. J., Jacobsen, S. D., Hauri, E. H., & Saal, A. E. (2013). Degassing

of reduced carbon from planetary basalts. *Proceedings of the National Academy of Sciences, 110* (20), 8010-8013. https://doi.org/10.1073/pnas.1219266110

Wieczorek, M. A., Neumann, G. A., Nimmo, F., Kiefer, W. S., Taylor, G. J., Melosh, H. J., Phillips, R. J., Solomon, S. C., et al. (2013). The Crust of the Moon as seen by GRAIL. *Science, 339* (6120), 671-675. https://doi.org/10.1126/science.1231530

Williams, D. A., Fagents, S. A., & Greeley, R. (2000). A reassessment of the emplacement and erosional potential of turbulent, low-viscosity lavas on the Moon. *Journal of Geophysical Research: Planets, 105* (E8), 20189-20205. https://doi.org/10.1029/1999JE001220

Wilson, L. (1972). Explosive Volcanic Eruptions – II The Atmospheric Trajectories of Pyroclasts. *Geophysical Journal of the Royal Astronomical Society, 30*, 381-392. https://doi.org/10.1111/j.1365-246X.1972.tb05822.x

Wilson, L. (1980). Relationships between pressure, volatile content and ejecta velocity in three types of volcanic explosion. *Journal of Volcanology and Geothermal Research,* 8 (2-4), 297-313. https://doi.org/10.1016/0377-0273(80)90110-9

Wilson, L., & Head, J. W. (1981). Ascent and Eruption of Basaltic Magma on the Earth and Moon. *Journal of Geophysical Research, 86* (NB4), 2971–3001. https://doi.org/10.1029/JB086iB04p02971

Wilson, L., & Head, J. W. (2003). Deep generation of magmatic gas on the Moon and implication for pyroclastic eruptions. *Geophysical Research Letters, 30* (12), 1605–1609. https://doi.org/10.1029/2002GL016082

Wilson, L., & Head, J. W. (2017). Generation, ascent and eruption of magma on the Moon: New insights into source depths, magma supply, intrusions and effusive/explosive eruptions (Part 1: Theory). *Icarus, 283*, 146–175. https://doi.org/10.1016/j.icarus.2015.12.039

Wilson, L., & Head, J. W. (2018). Controls on Lunar Basaltic Volcanic Eruption Structure and Morphology: Gas Release Patterns in Sequential Eruption Phases. *Geophysical Research Letters, 45* (12), 5852-5859. https://doi.org/10.1029/2018GL078327

Wilson, L., Mouginis-Mark, P. J., Tyson, S., Mackown, J., & Garbeil, H. (2009). Fissure eruptions in Tharsis, Mars: Implications for eruption conditions and magma sources. *Journal of Volcanology and Geothermal Research, 185* (1-2), 28-46. https://doi.org/10.1016/j.jvolgeores.2009.03.006

Yoshida, S., & Koyaguchi, T. (1999). A new regime of volcanic eruption due to the relative motion between liquid and gas. *Journal of Volcanology and Geothermal Research, 89* (1-4), 303-315. https://doi.org/10.1016/S0377-0273(99)00005-0

1511   Zein A., Hantke M., & Warnecke, G. (2010). Modeling phase transition for compressible two-
1512   phase flows applied to metastable liquids. *Journal of Computational Physics, 229* (8), 2964-
1513   2998. https://doi.org/10.1016/j.jcp.2009.12.026
1514
1515   Zolotov, M. Y. (2010). On the chemistry of mantle and magmatic volatiles on Mercury. *Icarus,*
1516   *212* (1), 24-41. https://doi.org/10.1016/j.icarus.2010.12.014

Figure 1.

a Pressure

25 ppm H_2O, 25 ppm CO
1500 ppm H_2O, 1500 ppm CO

b Temperature

c Mixture velocity

d Gas-slip velocity

e Viscosity

f Deborah number

Figure 2.

Figure 3.

a Pressure

b Temperature

c Mixture velocity

Legend:
- 2 ppm H$_2$, 25 ppm CO (blue)
- 84 ppm H$_2$, 1500 ppm CO (red)

d Gas-slip velocity

e Viscosity

f Deborah number

Figure 4.

a Exsolved gas volume fraction

b Dissolved H₂O content

c Dissolved CO content

Legend (panel a):
H₂O 25 ppm, CO 25 ppm
- - - H₂O
- - - CO
- - - Total gas
H₂O 1500 ppm, CO 1500 ppm
——— H₂O
——— CO
——— Total gas

d Exsolved gas volume fraction

e Dissolved H₂ content

f Dissolved CO content

Legend (panel d):
H₂ 2 ppm, CO 25 ppm
- - - H₂
- - - CO
- - - Total gas
H₂ 84 ppm, CO 1500 ppm
——— H₂
——— CO
——— Total gas

Figure 5.

a

Exsolved gas volume fraction

Depth (m)

H$_2$O 25 ppm, CO 25 ppm
— — H$_2$O
— — CO
— — Total gas
H$_2$O 1500 ppm, CO 1500 ppm
—— H$_2$O
—— CO
—— Total gas

b

Exsolved gas volume fraction

Depth (m)

H$_2$ 2 ppm, CO 25 ppm
— — H$_2$
— — CO
— — Total gas
H$_2$ 84 ppm, CO 1500 ppm
—— H$_2$
—— CO
—— Total gas

Figure 6.

Figure 7.

Figure 8.

a Exit gas volume fraction	**b** Mass flow rate	**c** Exit velocity	**d** Exit pressure
e Exit gas volume fraction	**f** Mass flow rate	**g** Exit velocity	**h** Exit pressure

Legend (top): Press., Temp., Radius, H_2O, CO

Legend (bottom): Press., Temp., Radius, H_2, CO

Figure 9.

Figure 10.